

5-2018

Design, Modeling, and Control of a Flying-Insect-Inspired Quadrotor with Rotatable Arms

Jin Hu
Purdue University

Follow this and additional works at: https://docs.lib.purdue.edu/open_access_theses

Recommended Citation

Hu, Jin, "Design, Modeling, and Control of a Flying-Insect-Inspired Quadrotor with Rotatable Arms" (2018).
Open Access Theses. 1396.
https://docs.lib.purdue.edu/open_access_theses/1396

This document has been made available through Purdue e-Pubs, a service of the Purdue University Libraries.
Please contact epubs@purdue.edu for additional information.

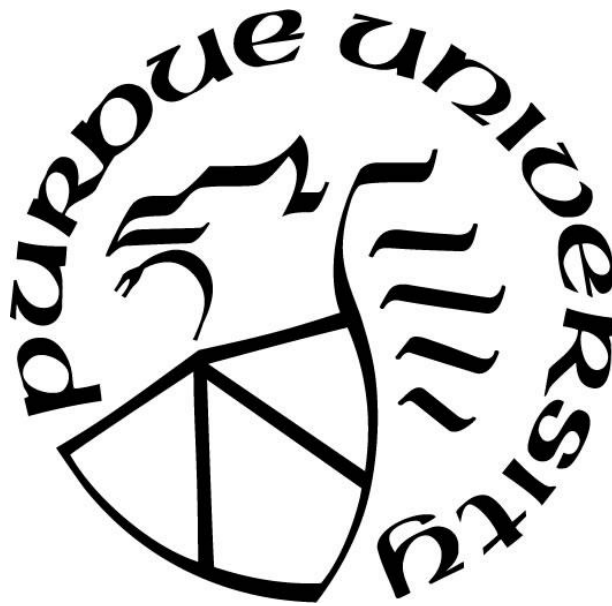
**DESIGN, MODELING, AND CONTROL OF
A FLYING-INSECT-INSPIRED QUADROTOR
WITH ROTATABLE ARMS**

by
Jin Hu

A Thesis

*Submitted to the Faculty of Purdue University
In Partial Fulfillment of the Requirements for the degree of*

Master of Science



School of Engineering Technology

West Lafayette, Indiana

May 2018

THE PURDUE UNIVERSITY GRADUATE SCHOOL
STATEMENT OF COMMITTEE APPROVAL

Dr. Xiumin Diao, Chair

School of Engineering Technology

Dr. Mark French

School of Engineering Technology

Dr. Byung-Cheol Min

Department of Computer and Information Technology

Approved by:

Dr. Duane D. Dunlap

Head of the Graduate Program

Dedicated to my family.

ACKNOWLEDGMENTS

Special thanks to my advisor, Prof. Xiumin Diao, for guidance and support in the last two years. I feel grateful and lucky to have him as my academic advisor.

I would also like to thank my parents for encouragement, the committee members, Prof. Mark French and Prof. Byung-Cheol Min for constructive comments, my lab mates and friends, Hao Xiong, Yuxin Liang, Lin Zhang, Yu Mei, Shengchao Li, and Hongyi Xu for help and friendship.

TABLE OF CONTENTS

LIST OF TABLES	viii
LIST OF FIGURES	ix
GLOSSARY	xi
LIST OF ABBREVIATIONS.....	xii
ABSTRACT.....	xiii
CHAPTER 1. INTRODUCTION	1
1.1 Background and Motivation	1
1.2 Scope.....	4
1.3 Significance	4
1.4 Research Questions.....	5
1.5 Assumptions.....	6
1.6 Limitations	7
1.7 Delimitations.....	7
1.8 Summary.....	8
CHAPTER 2. REVIEW OF LITERATURE	9
2.1 Dynamics modeling and control of QFAs	9
2.2 The displacement of the CoG for UAVs	10
2.3 Bio-inspired aerial robots.....	13
2.4 Summary.....	15
CHAPTER 3. RESEARCH METHODOLOGY	17
3.1 Modeling of the QRA	17
3.1.1 Kinematics of a QRA.....	21

3.1.2 Dynamics of a QRA in rotation	22
3.1.3 Dynamics of a QRA in Translation.....	23
3.2 Thrust Distribution Optimization for Energy Efficiency.....	23
3.3 Prototype Design.....	24
3.3.1 Frame	26
3.3.2 Flight Controller.....	28
3.3.3 Propulsion System and Power Supply	29
3.3.4 Arm Driving system.....	31
3.3.5 Wireless Kit, and External Sensors.....	34
3.4 Control Strategy	36
3.4.1 Flight controller	37
3.4.2 Arm rotation controller	40
3.4.2.1 Calculating the Bias Torque.....	41
3.4.2.2 Calculating Target Arm-Associated Angles	42
3.5 Summary	43
CHAPTER 4. RESULTS	44
4.1 Mapping from PWM signals to thrust of the BLDC motor	47
4.2 Mapping from the thrust to the power consumption of BLDC motor	48
4.3 Validation of the Arm Rotation Control (ARC)	49
4.4 Energy Consumption	53
4.5 Summary	54
CHAPTER 5. SUMMARY, CONCLUSIONS, and RECOMMENDATIONS	55
5.1 Conclusion	55
5.2 Recommendations.....	55

LIST OF REFERENCES	56
APPENDIX A. Program Code.....	63

LIST OF TABLES

<i>Table 3.1</i> Specifications of Daya 550 Frame.....	28
<i>Table 3.2</i> Propeller parameters	33
<i>Table 3.3</i> Weight of each part of the QRA	36
<i>Table 3.4</i> PID parameters of the QRA.....	39
<i>Table 4.1</i> Experiments with 10×4.7 propeller	46
<i>Table 4.2</i> Experiments with 11×4.7 propeller	46
<i>Table 4.3</i> Parameters of the QRA in the experiment	50
<i>Table 4.4</i> Experiment results when the QRA hovering with the eccentric payload.....	53

LIST OF FIGURES

<i>Figure 1.1</i> (a) Aerial manipulation; and (b) Aerial delivery (Rossi & Rocco, 2016; Lee, 2016) ..	2
<i>Figure 1.2</i> (a) A bee with expanded wings; and (b) A bee with folded wings (Rose, 2012)	4
<i>Figure 1.3</i> (a) A QRA prototype; and (b) Arms of the QRA prototype are rotatable	4
<i>Figure 2.1</i> Quadrotor with moving mass control (Haus, et. al, 2017)	11
<i>Figure 2.2</i> Stanford Climbing and Aerial Maneuvering Platform (Pope et. al, 2017)	14
<i>Figure 2.3</i> Passive Mechanism for Quadrotor Perching (Doyle et. al, 2013)	15
<i>Figure 3.1</i> Mechanism of quadrotor (Choi & Ahn 2015).....	18
<i>Figure 3.2</i> Notations of quadrotor in side view	19
<i>Figure 3.3</i> Dynamics notations of quadrotor in top view.....	20
<i>Figure 3.4</i> Before arm rotation control	25
<i>Figure 3.5</i> After arm rotation control.....	26
<i>Figure 3.6</i> Daya 550 quadrotor frame (Alibaba Group, n.d.).....	27
<i>Figure 3.7</i> Automatically folding and deploying mechanism for Daya 550	27
<i>Figure 3.8</i> Pixhawk Flight Controller (“Radiolink PixHawk Advanced Autopilot,” n.d)	29
<i>Figure 3.9</i> Propulsion system working process in QRA	30
<i>Figure 3.10</i> Propulsion system (“Turnigy Brushless Multi-Rotor Motor”, n.d.)	31
<i>Figure 3.11</i> Power supply (“ZIPPY Compact 5800mAh 4s 40c Lipo Pack”, n.d.)	31
<i>Figure 3.12</i> Exploded view of the arm-driving mechanism.....	33
<i>Figure 3.13</i> IMU data of Pixhawk and optical flow sensor	35
<i>Figure 3.14</i> Wireless kit and external sensors (Honegger, et. al, 2013)	36
<i>Figure 3.15</i> Control Strategy	37
<i>Figure 3.16</i> PID control experiment	39

<i>Figure 4.1</i> BLDC motor testing platform	45
<i>Figure 4.2</i> F/T sensor and user's interface ("ATI Industrial Automation", n.d.).....	45
<i>Figure 4.3</i> PWM versus thrust of BLDC motor.....	47
<i>Figure 4.4</i> Thrust versus the power of BLDC motor	49
<i>Figure 4.5</i> Field experiments	50
<i>Figure 4.6</i> Outputs when hovering with the payload at the symmetric center of quadrotor.....	51
<i>Figure 4.7</i> Outputs when hovering with the eccentric payload.....	52
<i>Figure 4.8</i> Power consumption.....	53

GLOSSARY

Conventional quadrotor - Quadrotor with fixed arms (QFA).

Eccentric payload - A payload is not located at the symmetric center of a quadrotor (Pounds, et. al, 2012).

F_B - Body-fixed frame fixed on the quadrotor (Pounds, et. al, 2010; Haus, et. al, 2017).

F_I - Inertial frame fixed on the ground (Pounds, et. al, 2010; Haus, et. al, 2017).

Displacement of CoG - The vector from the symmetric center to the CoG of the quadrotor in a body-fixed reference frame (Pounds, et. al, 2012).

Pulse-width modulation - A modulation technique used to encode a message into a digital pulsing signal. It is commonly used in electric control systems. By changing the PWM duty cycle, the power supply can be controlled to adjust the brushless motor speed or the rotation angle of the servo motor (Choi, & Ahn, 2015).

The centroid of the quadrotor body - The symmetric center projected onto the quadrotor plane (i.e. the x - y plane of F_B).

Unmanned aerial vehicle - Commonly known as a drone or unmanned aircraft system (UAS), is an aircraft without a human pilot aboard. “The flight of UAVs may operate with various degrees of autonomy: either under remote control by a human operator, or fully or intermittently autonomously, by onboard computers” (Tice, 1991).

LIST OF ABBREVIATIONS

APM - Ardupilot Mega

ARC - Arm Rotation Control

BLDC - Brushless Direct Current

CoG - Center of the Gravity

CPU - Central Processing Unit

DoF - Degree of Freedom

ESC - Electronic Speed Control

IMU - Inertial Measurement Unit

LiPo - Lithium Polymer

PID - Proportional- Integral- Derivative

PWM - Pulse-Width Modulation

QFA - Quadrotor with Fixed Arms

QRA - Quadrotor with Rotatable Arms

RPM - Revolutions Per Minute

SISO - Single-Input Single-Output

UAS - Unmanned Aircraft System

UAV - Unmanned Aerial Vehicle

ABSTRACT

Author: Hu, Jin. MS

Institution: Purdue University

Degree Received: May 2018

Title: Design, Modeling, and Control of a Flying-Insect-Inspired Quadrotor with Rotatable Arms

Major Professor: Xiumin Diao

Aerial manipulation and delivery using quadrotors are becoming more and more popular in recent years. However, the displacement of the center of gravity (CoG) is a common issue experienced by these applications due to various eccentric payloads carried. Conventional quadrotors with eccentric payloads are usually stabilized by robust control strategies through adjusting rotation speeds of BLDC motors, which has negative effects on stability and energy efficiency of quadrotors. In this thesis, a flying-insect-inspired quadrotor with rotatable arms is proposed. With four rotatable arms, the proposed quadrotor can automatically estimate the displacement of the CoG and drive the four arms to their optimal positions during flight. In this way, the proposed quadrotor can move its symmetric center to the CoG of the quadrotor with the eccentric payload to increase its stability and energy efficiency. The design, dynamics modeling, and control strategy of the proposed quadrotor are presented in this thesis. Both calculation and experiment results show that the proposed quadrotor with rotatable arms has better flight performance of stability and energy efficiency than the conventional quadrotor with fixed arms.

CHAPTER 1. INTRODUCTION

This chapter presents an overview of the study. The background, scope, significance, research questions, assumptions, limitations, and delimitations are discussed in this chapter.

1.1 Background and Motivation

An unmanned aerial vehicle (UAV) is an aircraft without a human pilot aboard. In recent years, UAVs have attracted a lot of attention in the robotics community. While they were initially designed for military purposes, researchers have found various applications of UAVs in many areas such as agriculture, movie-making, and recreation. Besides, the availability of many open source UAV controllers such as Ardupilot Mega (“ArduPilot Autopilot Suite,” 2016) and Pixhawk (“Pixhawk Autopilot,” 2017) further promotes the popularity of UAVs. A quadrotor is a kind of UAV that is propelled by four BLDC motors. Owing to their versatile maneuverability, low cost, and compact size, quadrotors have become very popular in many fields such as aerial manipulation and delivery (Hoffmann, et. al, 2004).

Aerial manipulation, as shown in Figure 1.1 (a), is implemented with one or more robotic manipulators installed on a quadrotor. The quadrotor manipulates objects using robotic manipulators. In recent years, researchers have developed various solutions to make aerial manipulation stable and efficient (Orsag, et. al, 2014; Kim, Choi, & Kim, 2013; Korpela, et. al, 2012). An adaptive controller for aerial manipulation was explored by (Orsag, et. al, 2014). A robotic arm was employed in aerial manipulation and the stability of the quadrotor with the robotic arm were discussed in (Kim, et. al, 2013; Korpela, et. al, 2012). Christopher et al. also researched aerial mobile manipulating (Korpela, et. al, 2012) and Fumagalli et al. explored the physical interaction of aerial manipulator with the environment (Fumagalli, et. al, 2014).

Aerial delivery, as shown in Figure 1.1 (b), is another promising application of quadrotors for commercial and rescue purposes. A team from Amazon Prime Air firstly delivered a commercial package using a quadrotor in 2016 (Amazon Prime Air, 2017). Researchers have also explored the trajectory generation of quadrotors with suspended payloads (Palunko, et. al, 2012) and the aerial delivery using multiple quadrotors (Mellinger, et. al, 2013). Aerial delivery was also reported for marine rescue (Yeong, et. al, 2015).

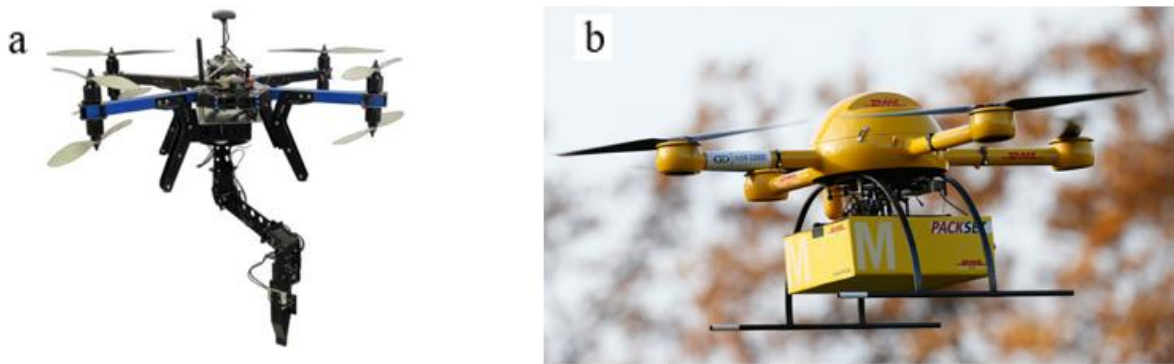


Figure.1.1 (a) Aerial manipulation; and (b) Aerial delivery (Rossi & Rocco, 2016; Lee, 2016)

Both aerial manipulation and delivery experience a common technical issue: the displacement of the Center of Gravity (CoG) of the quadrotor. The “displacement of CoG” is referred to the vector from the symmetric center to the CoG of the quadrotor in a body-fixed reference frame. When a quadrotor has no payload to carry or the payload carried is located at the symmetric center of the quadrotor, the CoG of the quadrotor system (i.e., the quadrotor together with the payload) coincides with the symmetric center of the quadrotor (Pounds, et. al, 2012). Therefore, the quadrotor can get the highest stability and energy efficiency (Rosen, et. al, 1989; Palunko, et. al, 2012). However, when the payload is not at the symmetric center of the quadrotor, the CoG of the quadrotor system will no longer stay at the symmetric center of the quadrotor (Pounds, et. al, 2012). Unlike human beings manipulating an object, conventional quadrotors used for aerial manipulation and delivery cannot eliminate such a displacement of the CoG by themselves

(Pounds, et. al, 2012). When a payload is not located at the symmetric center of a quadrotor, it is called an eccentric payload.

An eccentric payload introduces many issues for a conventional quadrotor that is referred to a quadrotor with fixed arms (QFA) in this thesis. The first issue is the decrease of stability. According to (Pounds, et. al, 2012; Rosen, et. al, 1989; Palunko, et. al, 2012), the response time to attitude and position control of a QFA carrying an eccentric payload was increased, which destabilized the QFA. The second issue is the increase of energy consumption. To have a stable attitude, a QFA has to produce different thrusts via changing the rotation speeds of its BLDC motors to balance the eccentric payload, which would decrease the overall energy efficiency of the QFA (Chovancová, et. al, 2014). Therefore, given the above issues caused by an eccentric payload, there has been consistent research efforts to minimize that the displacement of the CoG during flight of QFAs (Bartelds, et. al, 2016; Michael, et. al, 2011). More analyses on the displacement of the CoG are shown in chapter 3.

Inspired by flying insects (e.g., bees) that expand their wings when flying and hide them when crawling, as shown in Figure 1.2, I have proposed the concept of an automatically foldable aerial robot which has high potential applications in search and rescue (Hu, et. al, 2017). Based on this preliminary work on automatically foldable aerial robots, the design, modeling, and control of a quadrotor with rotatable arms (QRA) are discussed in this thesis. A prototype of the QRA is shown in Figure 1.3 (a). Like a flying insect, a QRA has rotatable arms, which is shown in Figure 1.3 (b). By rotating arms, a QRA can move its symmetric center to its CoG while still keeping all BLDC motor thrusts the same during flight. In this way, the stability and energy efficiency of the QRA can be improved in hovering or low-speed translation, compared to a QFA with the same arms, weight, motors, and eccentric payloads.

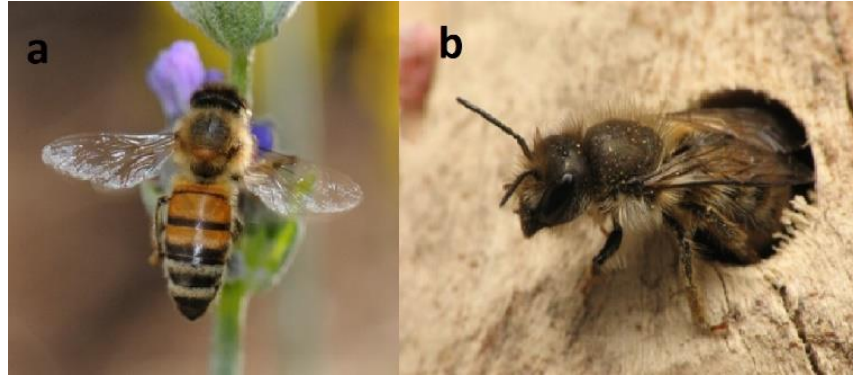


Figure 1.2 (a) A bee with expanded wings; and (b) A bee with folded wings (Rose, 2012)

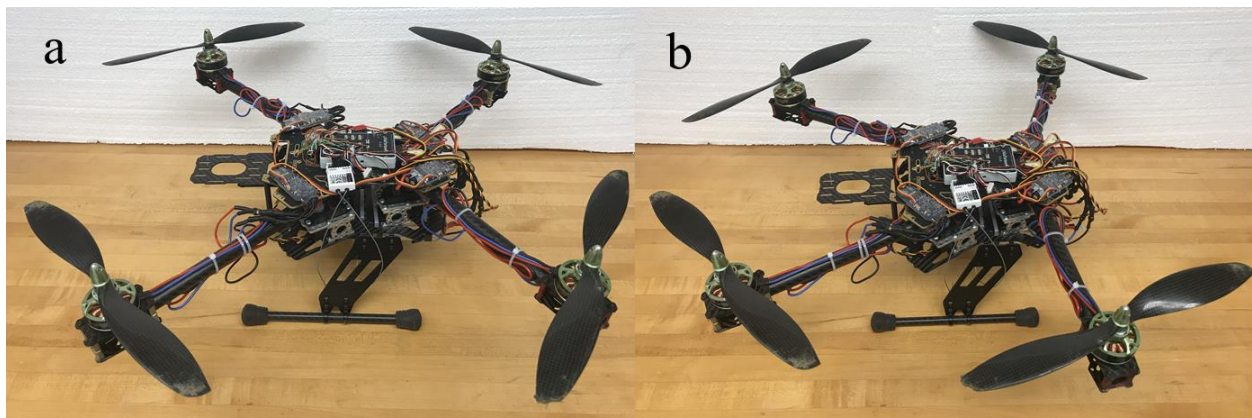


Figure 1.3 (a) A QRA prototype; and (b) Arms of the QRA prototype are rotatable

1.2 Scope

The proposed study covers the design, modeling, and control of a flying-insect-inspired QRA. Based on the design and control strategies developed in this study, simulations of the arm rotation control are conducted to verify the mathematical model of the QRA. Experiments on a prototype of the QRA are also conducted to validate theoretical analyses and simulations in this study.

1.3 Significance

To author's best knowledge, all academic research projects related to the displacement of the CoG of a quadrotor are focused on the development of robust flight control algorithms. The arms of the

quadrotors in prior research projects are always fixed. In other words, they cannot rotate during flight. However, the prior research on robust flight control algorithms of quadrotors is still challenging to keep the flight performance of stability and energy efficiency of quadrotor when compensating the displacement of the CoG.

In this study, the proposed QRA can compensate the displacement of the CoG by rotating its arms. Compared to the prior research on control algorithms of quadrotors, this method has improved the performance of stability and energy efficiency of a quadrotor with the displacement of the CoG.

Although the easiest way to eliminate the effects of the displacement of the CoG of a quadrotor is to extend the lengths of arms, a quadrotor with extended arms has larger size, which decreases the maneuverability and increases the manufacturing cost; Moreover, the larger the size of a quadrotor, the more energy it consumes during flight. The proposed QRA provides another solution for a quadrotor to handle the displacement of the CoG.

This research has three major contributions:

- Develop an algorithm to automatically identify the location of the CoG and a method to automatically transform a QRA by rotating its arms. In this way, the symmetric center of the QRA can be moved to the location of its CoG;
- Design and build a QRA prototype that can compensate the displacement of the CoG by rotating its arms in hovering or low-speed translation; and
- Validate the flight performance of stability and energy efficiency of the QRA experimentally.

1.4 Research Questions

The main research questions of this study are:

- How to develop an algorithm to identify the location of the CoG of a quadrotor with unknown payload?
- How to move the symmetric center to the location of the CoG of a quadrotor by rotating arms of QRA to optimal positions?
- How to design and build a QRA prototype?
- How to design experiments to validate the performance of the QRA on stability and energy efficiency?

1.5 Assumptions

The purpose of this study is to explore a flying-insect-inspired QRA and experimentally verify the improved energy efficiency and stability of such a quadrotor. The things that could affect the results of the study, but are not taken into account are:

- There is no collision or aerodynamic interference among propellers when the arms rotate. This is possible in practice because the arms of a quadrotor can always be designed longer. But in this study, only a specific length of arms is discussed.
- It is assumed that the voltage of the battery is assumed to be stable and it does not change during flight. It has been demonstrated that the voltage of the battery drops less than 5% on lithium polymer (LiPo) batteries discharged within 50% in (Dogger, 2011). Thus, the performance of brushless DC motors would not be influenced by the voltage drop in practice.
- All calculated data is obtained from the ideal scenario where there is no disturbance or vibration during simulation.

1.6 Limitations

The limitations of this study are:

- This research only discusses the performance of stability and energy efficiency of QRA in hovering and low-speed translation. Although the proposed QRA has potential applications in aerial delivery, the experiments in this study do not cover the situation that the quadrotor is in translation.
- The displacement of the CoG only happens on the quadrotor plane (i.e. x-y plane of F_B) in this study. The displacement of the CoG in the z axis of F_B may also affect the stability of the quadrotor during flight. But in this study, the offset in the z axis of F_B is not taken in to account.
- In this study, standard deviations of BLDC motor outputs are used to measure the stability of the quadrotor.

1.7 Delimitations

The delimitations of this study are:

- This study will not discuss other possible UAV systems such as multi-copter and fixed-wing UAVs. These UAV systems have totally different frames and dynamics models.
- Flying with a low-power battery (the discharge rate is below 50%) will not be taken into consideration for this study. If the battery discharge rate is below 50%, the voltage of the battery will decrease dramatically, which may distort the experiment data.
- For the proposed QRA, only hovering or low-speed translation is discussed with simulations and experiments.
- Ground effector of the quadrotor is not taken into account in the thesis.

1.8 Summary

This chapter presented an overview of the proposed research, which covers the background, motivation, scope, significance, research questions, assumptions, limitations, and delimitations of the study.

CHAPTER 2. REVIEW OF LITERATURE

To control a quadrotor or compensate the displacement of the CoG of the quadrotor, extensive studies have been done in recent years. This chapter presents an overview of prior works on dynamics modeling and control of the QFA, the displacement of the CoG for UAVs, and bio-inspired aerial robots.

2.1 Dynamics modeling and control of QFAs

Several approaches for mathematical modeling of the kinematics and dynamics of a QFA have been proposed by (Alaimo, et. al, 2013; Luukkonen, 2011). These models provided specific ways to control the attitude and position of QFAs.

The optimization of dynamics models has also been done by many researchers. (Bergamasco & Lovera, 2014) proposed an accurate continuous-time dynamics model for helicopters. This model had potential applications on closed-loop identification for helicopter operation. (Derafa, et. al, 2006) optimized the dynamics model of quadrotors to improve the flight stability and attitude precision, which demonstrated the effectiveness of the dynamics model by comparing simulation and experiment responses.

In practice, many uncertain situations (e.g., a gust) disturb quadrotors' normal operation. Intelligent adaptive control strategies were discussed by (Mohd, et. al, 2015). A non-linear multi-input multi-output quadrotor system was introduced. This study also designed a back-stepping control algorithm with a fuzzy compensator. The algorithm controls a quadrotor to track the desired trajectory. By calculating the fitness and error, the controller can automatically update the back-stepping control parameters. (Dydek, et. al, 2013) explored the control possibility of mitigating the effects of physical damage of UAVs.

In these studies, the energy efficiency of the dynamics system, namely, the energy consumption of BLDC motors and propellers, for a quadrotor has not been taken into account. Moreover, the frame of a quadrotor has always been assumed to be symmetric and fixed when developing the dynamics model in the prior research. Indeed, the mass distribution of a quadrotor is not always symmetric because of an extra payload or onboard equipment. Practically, it is hard to set the position of the CoG of the quadrotor together with the payload at the symmetric center of the quadrotor to eliminate the effects of the displacement of the CoG. Therefore, it is necessary to investigate the effects of a load offset on a quadrotor in the study.

2.2 The displacement of the CoG for UAVs

Because of the potential applications in aerial delivery and manipulation, researchers also explored the characteristics of the quadrotor when there is a displacement of the CoG.

Haus et al. proposed a novel method of shifting the CoG of a quadrotor to the symmetric center of the quadrotor and thus, one can maneuver the roll and pitch of the quadrotor efficiently (Haus, et. al, 2017). As shown in Figure 2.1, the CoG shifting was achieved via re-distributing an additional onboard weight. To shift the CoG back to the symmetric center of a quadrotor, the additional onboard weight usually has to be large enough, compared with the weight of the quadrotor and payloads. Although such a CoG shifting method could also be used to compensate the displacement of the CoG of a quadrotor, the large additional onboard weight can seriously reduce the payload capacity of the quadrotor.



Figure 2.1 Quadrotor with moving mass control (Haus, et. al, 2017)

Assuming that the CoG was at the symmetric center of the quadrotor, (Bristeau, et. al, 2009) discussed the role of the CoG location in flying stability. The position of the CoG can be either above or below the propeller disc plane (Quan, 2017). When a quadrotor in translation, if the CoG is below the propeller disc plane, the extra torque caused by the CoG will decrease the pitch angle that makes the quadrotor stable. However, no matter the CoG is above or below the propeller disc plane, it is hard to determine which situation is more stable under wind influence. When there is a gust, the torque generated by quadrotor gravity can either reject or accept the wind interference depending on the flying directions. (Pounds, et. al, 2010) also analyzed the unforced stability related to the height between motors and the CoG for their aerial platform X-4. They found that, when the height was coincident with the propeller plane, the system got the best stability.

Many adaptive controllers have been designed to compensate the displacement of the CoG. In (Antonelli, et. al, 2013), authors proposed a new algorithm to balance the parametric uncertainties and external disturbances automatically. Controller performance was also evaluated by various experiments when the quadrotor is attached with an unknown payload. (Ariyanto, & Naniwa, 2016) analyzed the mathematical model of a quadrotor with changing CoG. The impacts of the

CoG on UAV controller design were presented in (Kemper & Fatikow, 2006). This research addressed the potential control difficulties when sensors were not perfectly mounted at the CoG or the CoG was not located at the origin of the quadrotor's body-fixed frame.

The stability control of dynamic payloads (the CoG of quadrotor changes as time goes) using PID and permissible static imbalance torque has been investigated by (Pounds, et. al, 2012). They first came up with a stability model for an unmanned helicopter carrying an eccentric payload with a PID controller. Then, they applied this model to a quadrotor and pointed out, unlike a helicopter, the planar quadrotor imbalances were compensated by changing the relative proportion of the generated four thrusts. In order to stabilize the quadrotor, they trimmed the limited permissive static payload by the maximum changing speed of motors. This model proved that the permissive range of lateral offset for the quadrotor is far less than the conventional helicopter, which means the displacement of the CoG of the quadrotor is limited concerning to the stability.

Because quadrotors can reach the place where people have no access to, aerial manipulation is receiving more and more attention (Heredia, et al. 2014). People in building construction and rescue operations can benefit from the versatile maneuverability and controllability of the quadrotor. Despite the wide utilization of quadrotors in aerial manipulation, a few researchers have taken the displacement of the CoG of the quadrotor in to account (Heredia, et al. 2014).

Considering the displacement of the CoG caused by a robotic arm with two degrees of freedom in aerial manipulation, (Lee et. al, 2016) proposed an onboard balancing mechanism to increase the stability of the quadrotor. The balancing mechanism gained the control with respect to the movement of the onboard manipulator to balance the quadrotor with an eccentric payload. The improvement of robust attitude control was demonstrated. However, the additional mechanism in this study would significantly increase the energy consumption.

Research conducted by (Heredia, et al. 2014) proposed an admittance controller, called AMUSE, for aerial manipulation. In this research, cameras were used to assist with outdoor positioning. Unlike other controllers that are based on real-time data from IMU sensors, AMUSE control system highly relied on multi-camera motion captures, which provided the flying controller (Autopilot) precise attitude and position estimation. This control system extended the permissive range of the arm movement in aerial manipulation.

(Mellinger et. al, 2011) explored a possible aerial gripper for different locations of the CoG. The least-squares method was used to estimate the inertial parameters in hovering with a payload or disturbance. They also used the inertial parameters to estimate the lateral offset to compensate the controller.

Other than the controllers mentioned above, researchers have also developed other sophisticated flight control algorithms to control quadrotors considering the displacement of the CoG such as robust control (Nicol, et. al, 2011), sliding mode control (Zheng, et. al, 2014; Efe, 2011), backstepping techniques (Honglei, et. al, 2013; Choi & Bang, 2012; Madani & Benallegue, 2006; Das, et. al, 2009; Basri, et. al, 2015), impedance control (Fumagalli & Carloni, 2013), and task priority based control (Simetti & Casalino, 2016). All of these control methods have shown good results of quadrotor controlling. But when it comes to the displacement of the CoG of quadrotor, these methods still cannot avoid the decreased stability and energy efficiency.

2.3 Bio-inspired aerial robots

Inspired by natural creatures, many researchers have found methods to increase the energy efficiency of UAVs.

There was research analyzing a new type of hybrid aerial robot called HyTAQ (Kalantari & Spenko, 2014). It was a micro quadrotor encapsulated with a cage. Ball bearings were used for balancing the quadrotor and cage. The robot can alter the locomotion patterns from flying in the air to move on the ground. The battery life was elongated, which allowed the robot to execute tasks that require strong cruising abilities.

A group of researchers presented a multi-modal robot that was able to climb walls. Inspired by the lizard, a robot that is called Stanford Climbing and Aerial Maneuvering Platform (Pope et. al, 2017) is proposed as shown in Figure 2.2. This platform is equipped with a quadrotor with “two hands”, which allows the quadrotor to perch on a surface passively without any motion control. This innovation not only provided a battery efficiency solution for quadrotors but presented an alternative plan for climbing failure. If two “hands” could not provide sufficient friction force, the controller would command the propellers to rotate automatically until the quadrotor stabilize itself. This mechanism also allowed the extension of mission life by reducing power draw.

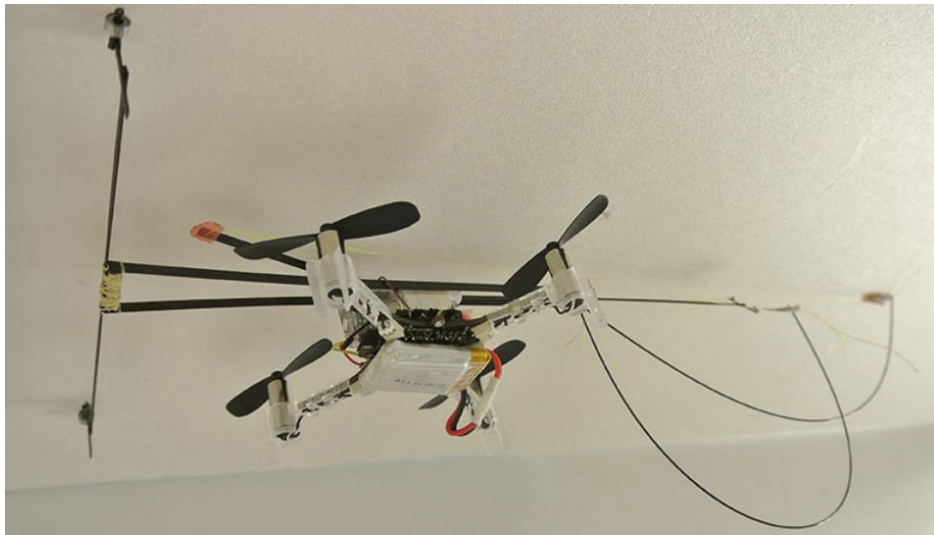


Figure 2.2 Stanford Climbing and Aerial Maneuvering Platform (Pope et. al, 2017)

The paper (Doyle et. al, 2013) introduced a passive stabilized mechanism for quadrotor flying, as shown in Figure 2.3. Inspired by a bird’s adaption to sleeping stably on trees without any force

control, researchers presented a detailed design of the passive stable mechanism. The robot, such as AVIAN, has legs and feet that allow the quadrotor to land anywhere. Using this mechanism, quadrotors could save energy dramatically compared to hovering in the air. Because the efficiency of a conventional quadrotor is low, this mechanism provided a solution that the quadrotor can stay on any surface without any power consumption to extend the battery life. As long as the quadrotor took off, the claw would naturally release. The robot imitated a bird relaxes on a branch, which also made it possible for a drone to recharge on the branch.

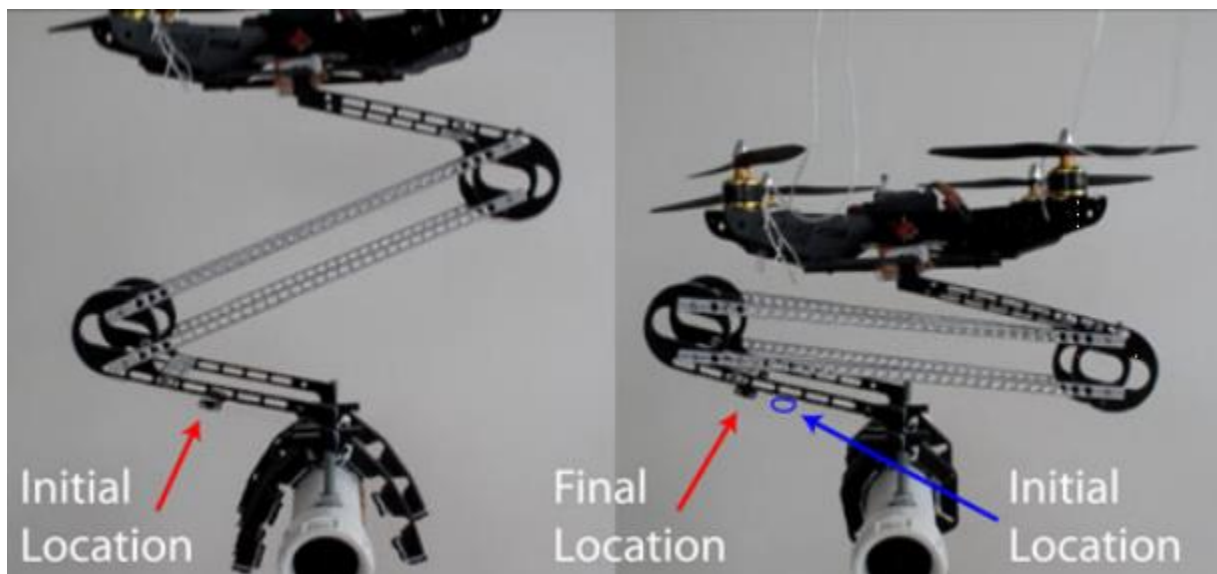


Figure 2.3 Passive Mechanism for Quadrotor Perching (Doyle et. al, 2013)

2.4 Summary

To the authors' best knowledge, when it comes to handling the issues caused by the eccentric payload of a quadrotor, the prior research has been following two conventions:

- The frame of a quadrotor is unchangeable. In other words, the quadrotor is treated as a rigid body and the arms of the quadrotor cannot rotate automatically during flight in purpose of compensating the displacement of the CoG.

- For a quadrotor carrying an eccentric payload, all the prior research relies on the flight controller to compensate the effects caused by the eccentric payload.

Although the existing solutions based on these two conventions can balance the eccentric payload carried by a quadrotor, one has to pay the price with decreased stability and lower energy efficiency of the quadrotor.

CHAPTER 3. RESEARCH METHODOLOGY

By rotating the arms, QRAs can move their symmetric center to their CoG while still keeping all BLDC motor thrusts the same during flight. In this way, the stability and energy efficiency of the QRAs can be improved in hovering or low-speed translational motion, compared to the QFAs with the same arms, weight, BLDC motors, and eccentric payloads. This chapter introduces the methodology of the study. It includes modelling of the QRA, thrust distribution optimization for energy efficiency, prototype design, and control strategy.

3.1 Modeling of the QRA

Before introducing the dynamics modeling of QRA, it is necessary to figure out the mechanism of the quadrotor that is shown in Figure 3.1 (Choi & Ahn, 2015). The maneuvers of the quadrotor are achieved by changing the thrust or torque generated by four BLDC motors. For example, to rotate clockwise or counterclockwise, a quadrotor needs to speed up diagonal BLDC motors. However, like most of the research of quadrotor, all these situations are based on a model that the payload is positioned at the symmetric center of the quadrotor. In other words, there is no displacement of the CoG. If an eccentric payload is taken into consideration, the maneuvers will become more complicated. More details are introduced in section 3.2.

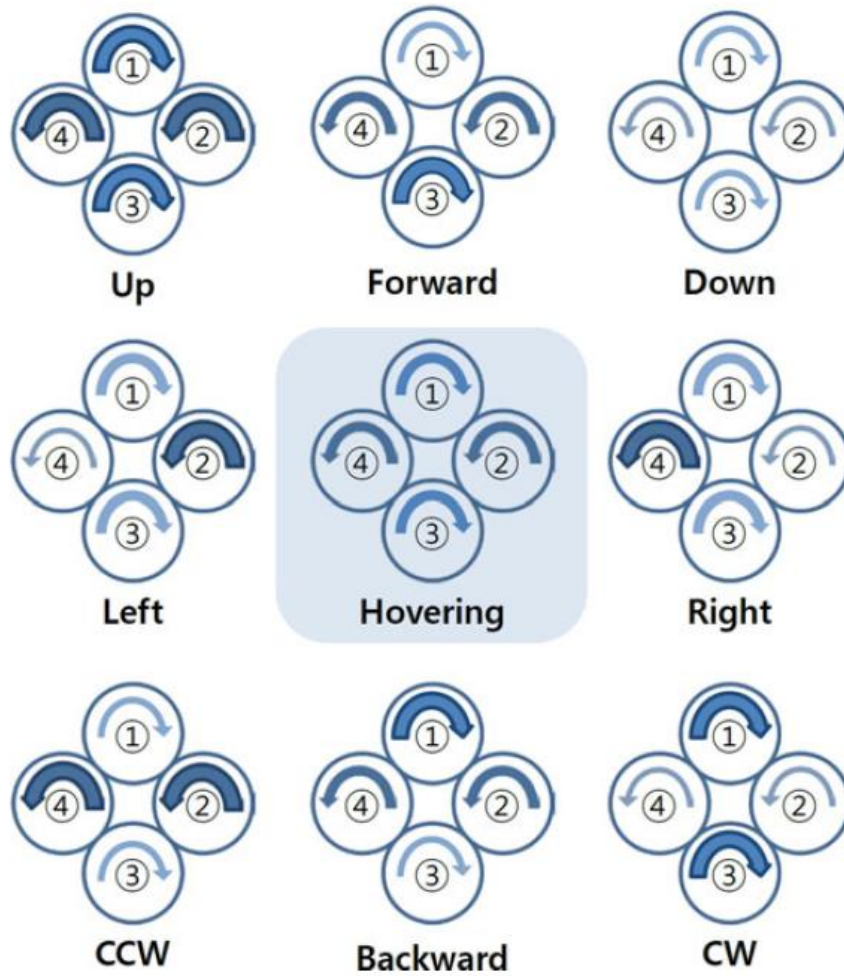


Figure 3.1 Mechanism of quadrotor (Choi & Ahn 2015)

Dynamics models of QFAs have been presented by several researchers (Bergamasco & Lovera, 2014; Luukkonen, 2011; Chovancová, et. al, 2014). In these studies, QFAs are assumed to be symmetric in both structure and mass distribution. In other words, the CoG offset of a QFA has not been taken into account in its dynamics model. However, in practice, the mass distribution of a QFA, as well as a QRA proposed in this thesis, is normally asymmetric because of the variation of payloads, onboard equipment, etc. Therefore, the CoG of a quadrotor is usually offset from the symmetric center of the quadrotor. In this study, a QRA structure is proposed and the CoG offset is taken into account in the dynamics modeling of the proposed QRA.

The dynamics notations of a QRA and the position of the axis of arm's rotation in F_B are shown in Figure 3.2 and Figure 3.3. Let F_I represents the inertial frame fixed on the ground and F_B represents the body-fixed frame fixed on the quadrotor. The origin of F_B locates at the centroid of the quadrotor body (arms are not included), and the rotation of arms does not affect the centroid of the quadrotor body. The attitude of F_B with respect to F_I is described by three Euler angles (i.e., roll, pitch, and yaw). The i th arm of the QRA is able to rotate about the i th axis which is perpendicular to the quadrotor plane (i.e. the x-y plane of F_B).

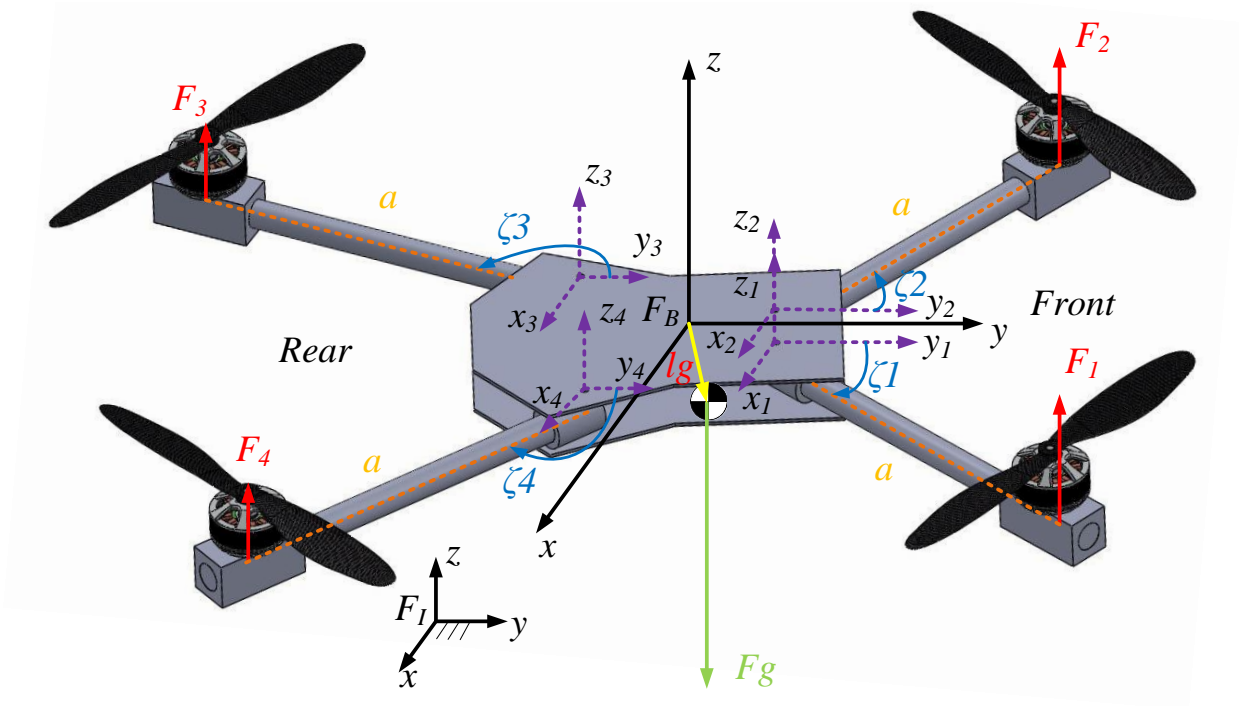


Figure 3.2 Notations of quadrotor in side view

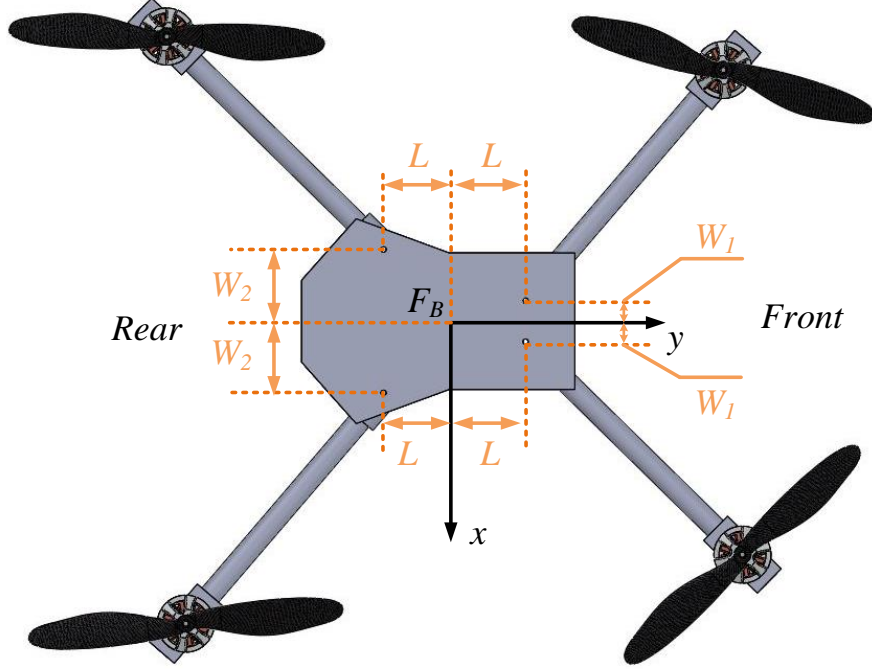


Figure 3.3 Dynamics notations of quadrotor in top view

Let ζ_i ($i = 1, 2, 3, 4$) represents the arm-associated angle of the i th arm of the QRA. An arm-associated angle is measured from the y axis of F_B to an arm of a quadrotor (Mahony, et. al, 2012). It should be noted that ζ_i ($i = 1, 2, 3, 4$) is a variable. In order to prevent collision of propellers of a QRA, the arm-associated angle ζ_i ($i = 1, 2, 3, 4$) can be limited to a certain range. All arms of the quadrotor are assumed to have the same length a . The length of an arm is the distance from the axis of the BLDC motor to the axis of the corresponding rotation. $\mathbf{l}_g = [l_x, l_y, l_z]^T$ is the position vector of the CoG of the quadrotor in F_B . $\mathbf{F}_g = [F_x, F_y, F_z]^T$ is the gravity of the quadrotor in F_B . Its magnitude is mg , where m is the total mass of the quadrotor and payload, and g is the gravitational acceleration. \mathbf{F}_i ($i = 1, 2, 3, 4$) represents the thrust of the i th BLDC motor in F_B . Its magnitude is denoted as F_i ($i = 1, 2, 3, 4$). The front of the QRA is along the y axis of F_B .

3.1.1 Kinematics of a QRA

The attitude of the quadrotor represented by F_B is described by three Euler angles, namely, roll ϕ , pitch θ , and yaw ψ , in F_I . The angular velocity of the quadrotor is denoted as $\boldsymbol{\eta} = [p \ q \ r]^T$ in F_B and $\mathbf{H} = [\dot{\phi}, \dot{\theta}, \dot{\psi}]^T$ in F_I , respectively.

The transformation matrix from F_B to F_I is (Luukkonen, 2011),

$${}^I_B\mathbf{R} = \begin{bmatrix} C_\psi C_\theta & C_\psi S_\theta S_\phi - S_\psi C_\phi & C_\psi S_\theta C_\phi + S_\psi S_\phi \\ S_\psi C_\theta & S_\psi S_\theta S_\phi + C_\psi C_\phi & S_\psi S_\theta C_\phi - C_\psi S_\phi \\ -S_\theta & C_\theta S_\phi & C_\theta C_\phi \end{bmatrix} \quad (1)$$

where C_{angle} and S_{angle} are designated to denote $\cos(angle)$ and $\sin(angle)$, respectively. ${}^I_B\mathbf{R}$ is orthogonal, so the rotation matrix of a vector from F_I to F_B is (Luukkonen, 2011),

$${}^I_B\mathbf{R} = {}^B_I\mathbf{R}^{-1} = {}^B_I\mathbf{R}^T \quad (2)$$

The rotation matrix transforming the angular velocity of the quadrotor from F_B to F_I is (Luukkonen, 2011),

$${}^\eta_H\mathbf{R} = \begin{bmatrix} 1 & S_\phi T_\theta & S_\phi T_\theta \\ 0 & C_\phi & -S_\phi \\ 0 & \frac{S_\phi}{C_\theta} & \frac{C_\phi}{C_\theta} \end{bmatrix} \quad (3)$$

where T_{angle} is designated to denote $\tan(angle)$. The rotation matrix transforming the angular velocity of the quadrotor from F_I to F_B is (Luukkonen, 2011),

$${}^H_\eta\mathbf{R} = \begin{bmatrix} 1 & 0 & -S_\theta \\ 0 & C_\phi & C_\theta S_\phi \\ 0 & -S_\phi & C_\theta C_\phi \end{bmatrix} \quad (4)$$

Assume the BLDC motors and the propellers on the quadrotor are the same in the study. The thrust generated by the i th BLDC motor in F_B can be expressed as (Chovancová, et. al, 2014),

$$\mathbf{F}_i = k_t \omega_i^2 \quad (5)$$

3.1.2 Dynamics of a QRA in rotation

The dynamics model of a quadrotor in this thesis is derived based on the dynamics models of QFAs presented in (Bergamasco & Lovera, 2014; Luukkonen, 2011; Chovancová, et. al, 2014).

In this study, the bias torque caused by the displacement of the CoG of a quadrotor, denoted as $\boldsymbol{\tau}_g$, is included in the dynamics model. The dynamics equation governing the rotation of a quadrotor with respect to F_B can be expressed as,

$$\mathbf{I}_q \dot{\boldsymbol{\eta}} + \boldsymbol{\eta} \times \mathbf{I}_q \boldsymbol{\eta} = \boldsymbol{\tau}_r + \boldsymbol{\tau}_g + \boldsymbol{\tau}_{gyro} + \boldsymbol{\tau}_\eta \quad (6)$$

where \mathbf{I}_q is the moment of inertia matrix of the quadrotor in F_B . It should be pointed out that, because of the displacement of the CoG, \mathbf{I}_q is not necessarily a diagonal matrix. Since the BLDC motors and arms of a quadrotor are usually much lighter than the quadrotor and payload, it is assumed in the thesis that \mathbf{I}_q does not change with the rotation of the QRA's arms. $\dot{\boldsymbol{\eta}}$ is the angular acceleration of the quadrotor with respect to F_B . $\boldsymbol{\eta} \times \mathbf{I}_q \boldsymbol{\eta}$ is the centrifugal torque. $\boldsymbol{\tau}_{gyro}$ is the gyroscopic torque. $\boldsymbol{\tau}_\eta$ is the rotational aerodynamic drag (Chovancová, et. al, 2014). The bias torque, $\boldsymbol{\tau}_g = [\tau_{gx}, \tau_{gy}, \tau_{gz}]^T$, can be expressed as,

$$\boldsymbol{\tau}_g = \mathbf{l}_g \times \mathbf{F}_g \quad \text{or} \quad \begin{bmatrix} \tau_{gx} \\ \tau_{gy} \\ \tau_{gz} \end{bmatrix} = \begin{bmatrix} l_y F_z - l_z F_y \\ l_z F_x - l_x F_z \\ l_x F_y - l_y F_x \end{bmatrix} \quad (7)$$

$\boldsymbol{\tau}_r$ is the torque generated by all BLDC motor thrusts, and it can be expressed as,

$$\boldsymbol{\tau}_r = \begin{bmatrix} \tau_{rx} \\ \tau_{ry} \\ \tau_{rz} \end{bmatrix} = \begin{bmatrix} a \sum_{i=1}^4 \cos \zeta_i F_i + L \sum_{i=1}^2 F_i - L \sum_{i=3}^4 F_i \\ a \sum_{i=1}^4 \sin \zeta_i F_i + W_1 \sum_{i=1}^2 (-1)^i F_i - W_2 \sum_{i=3}^4 (-1)^i F_i \\ \sum_{i=1}^4 (-1)^i \tau_{di} \end{bmatrix} \quad (8)$$

where $\tau_{di}(i = 1,2,3,4)$ is the drag torque generated by the i th motor in F_B due to the rotation of the i th propeller. According to (Rinaldi, et. al, 2013) $\tau_{di}(i = 1,2,3,4)$ is approximately proportional to $F_i(i = 1,2,3,4)$ when the quadrotor has a stable attitude (e.g., hovering and low-speed translational motion).

3.1.3 Dynamics of a QRA in Translation

The dynamics equation governing the translation of a quadrotor in F_B can be expressed as (Chovancová, et. al, 2014)

$$m\dot{\mathbf{v}} + \boldsymbol{\eta} \times m\mathbf{v} = \mathbf{F}_r + \mathbf{F}_g + \mathbf{F}_v \quad (9)$$

where \mathbf{v} and $\dot{\mathbf{v}}$ are the velocity and acceleration of the quadrotor with respect to F_B . \mathbf{F}_r is the total thrust generated by all four BLDC motors. \mathbf{F}_v is the translational aerodynamic drag.

3.2 Thrust Distribution Optimization for Energy Efficiency

QFA compensates the bias torque by generating different BLDC motor thrusts. Such thrust distribution of QFA decreases the energy efficiency of the quadrotor. The proposed QRA can redistribute the thrust by rotating arms and the energy efficiency of quadrotor benefits from that. This chapter discusses the energy efficiency optimization of thrust distribution of QRA.

For BLDC motor, it has been proposed that the power consumption is a function of thrust in (Atlam & Kolhe, 2013),

$$P_r = f(F) = K_p F^{1.5} \quad (10)$$

where P_r is the power consumption of the BLDC motor, F is the generated thrust, and K_p is a BLDC motor and propeller-dependent coefficient.

If a quadrotor is in a stable state (i.e., hovering or low-speed translation), then the thrusts generated by all BLDC motors can be described as,

$$F_r = \sum_{i=1}^4 K_F \omega_i^2 \quad (i = 1, 2, 3, 4) \quad (11)$$

where k_F is the thrust constant, ω_i is the angular velocity of i th BLDC motor.

The sum of the power consumptions of the quadrotor is described as

$$P_q = \sum_{i=1}^4 P_i = \sum_{i=1}^4 K_p (K_F \omega_i^2)^{1.5} \quad (12)$$

Based on Cauchy-Schwarz Inequality in (Zygmund, 1953), one has,

$$P_q = \sum_{i=1}^4 K_p (K_F \omega_i^2)^{1.5} \geq \frac{K_p}{4} \sum_{i=1}^4 (K_F \omega_i^2)^{0.75} \quad (13)$$

With equality holding if and only if the ω_i are all equal. Therefore, the minimum of power consumption, namely, the best energy efficiency, of the quadrotor in a stable state is achieved if the ω_i are all equal. If I can keep the four BLDC motors running at the same angular velocity when carrying eccentric payloads, the quadrotor will get the highest energy efficiency.

Thus, for the QRA, the general idea of arm rotation control is to re-distribute the thrust by rotating the arms to the target positions to enable the four BLDC motors of quadrotor to remain the same rotation speed when carrying an eccentric payload.

3.3 Prototype Design

The QRA can move the symmetric center to its CoG by the arm's rotation, while still keeping all BLDC motor thrusts the same during flight. The rotation process in a simplified model can be described as follows. In Figure 3.4, F_i ($i=1,2,3,4$) denotes the corresponding thrusts for i th ($i=1,2,3,4$) motor. The names of four arms of the quadrotor also follow this regulation. To compensate the displacement of the CoG, motors 1 and 2 speed up initially. At this time, F_1 and F_2

are greater than $mg/4$ while F_3 and F_4 are less than $mg/4$. Then, by rotating arms 3 and 4 with angles ζ_3 and ζ_4 , respectively, the QRA can re-distribute four thrusts and make four motors generate equal thrusts ($F_i (i=1,2,3,4) = mg/4$), as shown in Figure 3.5. In this way, the four angular velocities of BLDC motors can remain the same even if the quadrotor has an eccentric payload. This section introduced the prototype of the QRA that can realize the function introduced above. The components of QRA include a frame, controller, propulsion system, power supply, arm drive, wireless kit, and external sensors. Details of each component are illustrated as follows,

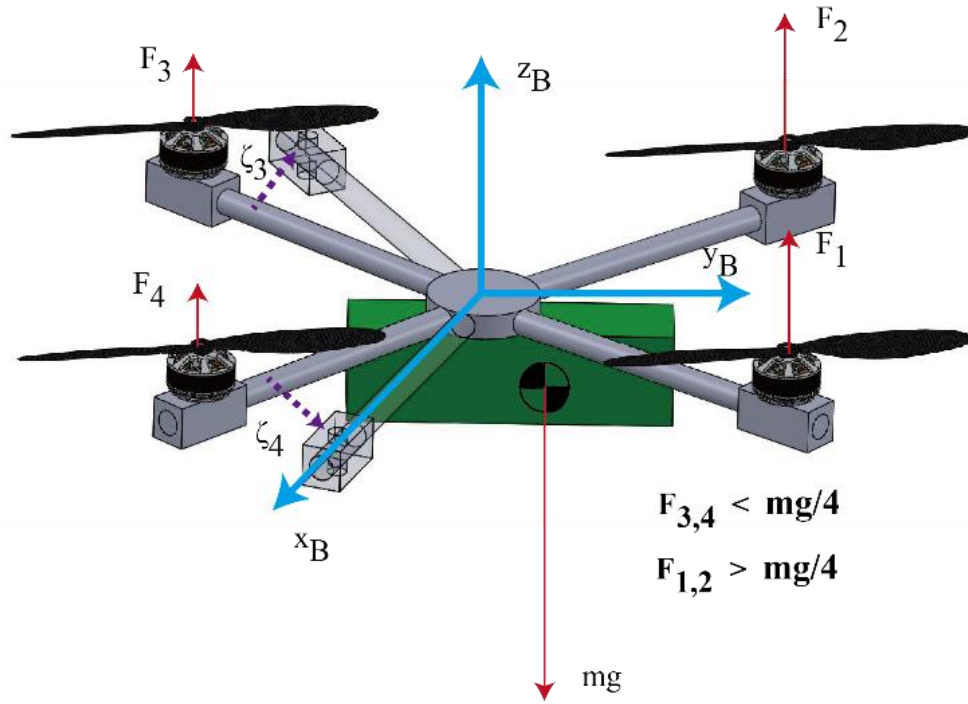


Figure 3.4 Before arm rotation control

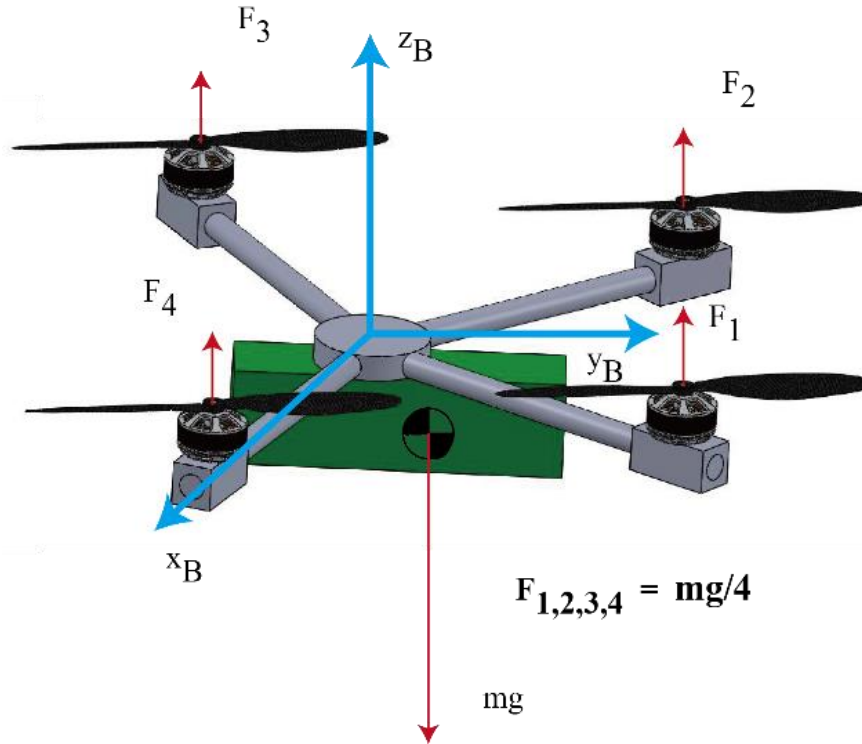


Figure 3.5 After arm rotation control

3.3.1 Frame

In the preliminary work (Hu, Liang, & Diao, 2017) of the thesis, Daya 550 in Figure 3.6 was redesigned to make the frame automatically fold and deploy. A crank-slider mechanism was used to convert the rotary motion of the servo motor to translational motion of the sliders, as shown in Figure 3.7. By rotating the crank, the sliders were pulled back and forth to either fold or deploy the frame. The mechanism was driven by one servo motor, which rotates the crank mechanisms to push all four arms.



Figure 3.6 Daya 550 quadrotor frame (Alibaba Group, n.d.)

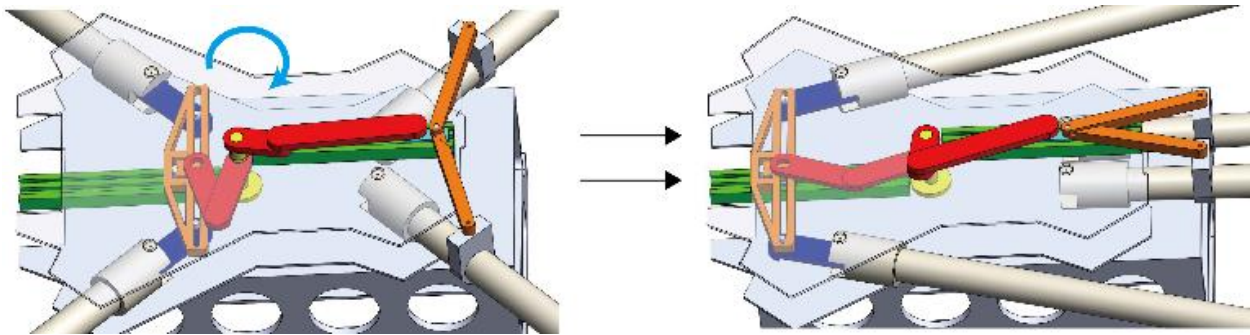


Figure 3.7 Automatically folding and deploying mechanism for Daya 550

In this study, a light-weight and durable arm driven system that allows the QRA easily rotate its arms during flight is designed. For the purpose of arm rotation, I select the Daya 550 frame (DAYA, Shenzhen, China) whose arms can be rotated manually. Each arm of the Daya 550 frame can rotate with respect to the frame independently. This frame provides easy access to its inner space, which makes it convenient to build the prototype of the QRA. For the purpose of light-weight and durable, Daya 550 frame is made of carbon fiber, which has great strength to weight ratio ($2,457 \text{ kN} \cdot \text{m/kg}$). More details of specifications of Daya 550 frame are shown in Table 3.1,

Table 3.1 Specifications of Daya 550 Frame

Name	Value	Unit
Wheelbase	550	mm
Inner space height	22	mm
Higher landing gear	15	cm
Arm diameter	16	mm
Material thickness	1.5	mm
Weight	380	g

3.3.2 Flight Controller

Pixhawk, as shown in Figure 3.8, is chosen as the embedded processor of the QRA. It is a reliable open-source microcontroller designed for the high-end autopilot. This processor owns a 32bit CPU, which has powerful process capability for fast response of flight and arm rotation control. It also owns an onboard IMU sensor that can get the acceleration in three-dimensional space in real time. Moreover, Pixhawk also provides enough communication ports to expand its functions. For example, the analog control and I2C ports are used for the QRA localization during the experiment at loiter. Eight PWM outputs also make Pixhawk possible to control both BLDC motors and servo motors. The 1st - 4th output channels are used for BLDC motors control and the 5th -8th output channels are assigned for servo motor control. Pixhawk's size is portable ($L \times W \times H$: 81.5×50×15.5 mm) and it has only 38 g weight, which is ideal for the QRA.

Pixhawk also has abundant libraries for sensors and data analysis. It is convenient to merge some libraries with users' program to validate the arm rotation control (ARC) strategy. More details of the programming libraries will be introduced in Section 3.4.



Figure 3.8 Pixhawk Flight Controller (“Radiolink PixHawk Advanced Autopilot,” n.d)

3.3.3 Propulsion System and Power Supply

The propulsion system determines the flight performances of the QRA (Quan, 2017). It includes BLDC motors, electronic speed controllers (ESCs) and propellers, as shown in Figure 3.10.

BLDC motor, also called electronically commutated motors, has high speed, high power to weight ratio, and outstanding electronic control ability. It has been widely used as the motor of multi-copter. Turnigy V3508-KV580 BLDC motors (FLYSKY, Shenzhen, China) are selected considering the high permissive payload requirements of the QRA experiments. This BLDC motor can provide over 10 N thrust and the weight of this BLDC motor is 97 g. I use HobbyKing 30 A BlueSeries (FLYSKY, Shenzhen, China) for the ESCs of the QRA since its maximum continuous current of this BLDC motor can reach 25 A. The propellers selection is related to not only the energy efficiency of the quadrotor but also the rotation scope of each arm. The larger size of propeller typically has a better performance of the energy efficiency of the quadrotor. However, enough space is needed to be reserved to avoid potential collision between propellers during the rotation of arms. Therefore, 11×4.7 carbon fiber propellers are selected whose size is 10-inch diameter with a pitch of 4.7 inches per revolution. It allows each arm to rotate within $\pm 20^\circ$ from its original position without any interference. The power supply also needs to match with the

BLDC motors and ESCs. Thus, the whole QRA is powered by a four-cell 5800 mA·h 40 c Lipo battery in Figure 3.11.

In QRA, each BLDC motor is powered and controlled by an ESC independently. After the ESC receiving the pulse-width-modulation (PWM) signal commended by the controller, ESCs transmit the power with corresponding frequency to the BLDC motor to control their rotation speed ω and the torque. In other words, the ESC provides pulses of power to control the speed and torque of BLDC motor. However, this kind of control is not linear. Several experiments are designed in this study to figure out the properties of BLDC motors and they will be introduced in chapter 4 Experiment results.

The power module is installed between the battery and other electrical components. It has two main functions in this study:

- Provides a stable 5.37 V and 2.25 A power supply to the flight controller.
- Measures the voltage and the current of the battery and triggers auto-landing when the voltage becomes lower than the threshold. The power module can work when the voltage of the power supply is below to 18 V and the maximum current is 90 A.

Figure 3.9 shows how the electrical propulsion system works in QRA.

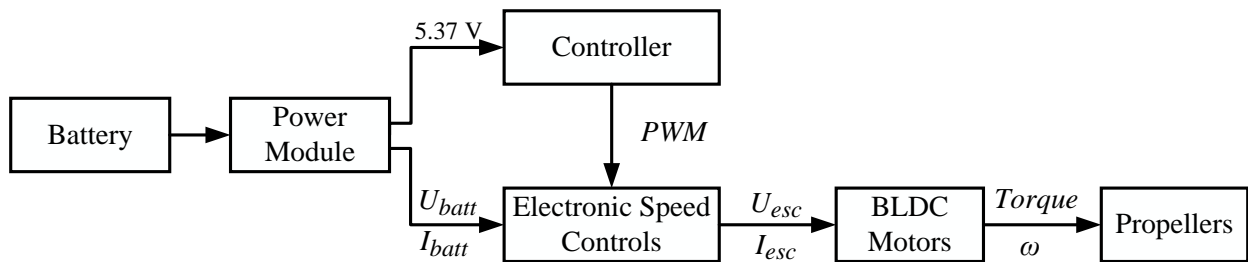


Figure 3.9 Propulsion system working process in QRA



Figure 3.10 Propulsion system (“Turnigy Brushless Multi-Rotor Motor”, n.d.)



Figure 3.11 Power supply (“ZIPPY Compact 5800mAh 4s 40c Lipo Pack”, n.d.)

3.3.4 Arm Driving system

The arms of QRA can rotate independently, each of which is driven by a servo motor. A servo motor is a DC motor coupled to an encoder. Thus, it allows for precise control rotation position in a close-loop. Although the sensor in the servo motor can only provide position feedback, the speed of servo motor can also be controlled by signal frequency. The signal that is used for servo motor control is Pulse Width Modulation (PWM) signal. PWM signal is a kind of square wave that intermittently switch the signal. The duty cycle of PWM is expressed in percent. 0% is referred to fully off while 100% is referred to fully on. By adjusting the duty cycle, PWM can control the position of the servo motor. For example, PWM signal in servo motor control is within 1000-2000 μ s, which has corresponding duty cycle of 0% to 100%. The neutral position of the servo motor is

set when the PWM signal is 1,500 μ s. In this case, when the duty cycle is less than 50%, the servo motor rotates clockwise, and vice versa. The rotation angle is linear to the duty cycle. Thus, to implement the QRA arm driven system, PWM signal makes it possible to get an analog result in a digital way.

For the servo motor, there are three cables to power and control the servo motor. One is for signal transmission and the other two are the power cable. The servo motors of QRA is directly powered and controlled by the embedded controller. Pixhawk can provide the power of 5.37 V to servo motors.

Figure 3.12 presents the exploded view of the arm driven system design. Servo motors are fixed on the Daya 550 frame using designed aluminum mounts. Each mount is composed of two stands and one block. 25T servo horns are used to connect servo motors and arms. Using servo horns, the servo motor and the arm are integrated together. Thus, the arms can be rotated to the target angles with the control of servo motor. To make the connections between servo motors and arms as reliable as possible, besides two threaded connections in each arm, a 30 mm bolt is also installed to avoid potential overwhelmed shear stress applied to the servo horn.

Hitec HS-645MG servo motors is chosen as the drive motor of arms. To avoid unexpected passive rotation of arms, the maximum torque that a servo can achieve has to exceed the torque generated by the BLDC motor. The estimated torque produced around the BLDC motor axis is given by (Chovancová, et. al, 2014),

$$D_i = c_p \rho \pi r^5 \omega^2 \quad (14)$$

where c_p is the power coefficient of the propeller, ρ is the air density, r is the radius of the propeller, and ω is the rotation speed of the BLDC motor. According to (Benito, et. al, 2014), and Table 3.2, one can calculate the maximum torque that BLDC motor can produce is 2.047 kg · cm. Note that

the HS-645MG servo motors can provide $7.7 \text{ kg} \cdot \text{cm}$ torque at 4.8 V , which exceeds the achievable torque of the BLDC motor at the highest rotation speed. Therefore, HS-645MG servo motors meet the torque requirement of the QRA.

Table 3.2 Propeller parameters

Name	Parameter	Value	Unit
Power coefficient of the propeller	c_p	0.04	-
Air density (15°C)	ρ	1.225	kg/m^3
Radius	r	0.1397	m
Maximum rotation speed	ω	5000	RPM

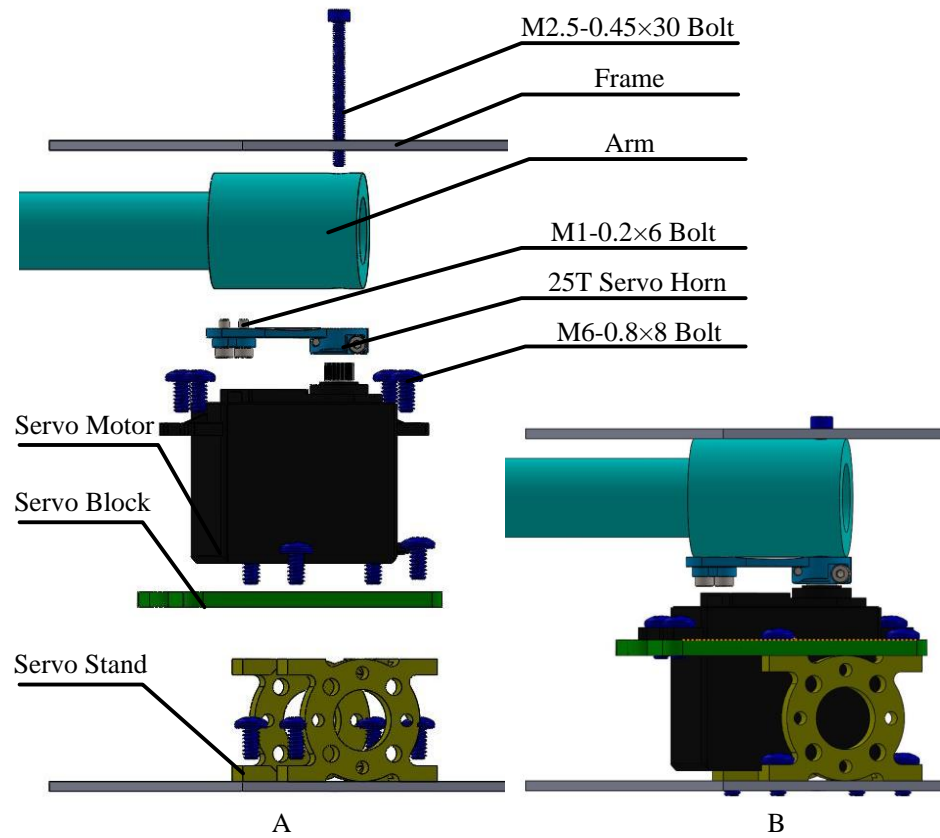


Figure 3.12 Exploded view of the arm-driving mechanism

3.3.5 Wireless Kit, and External Sensors

The wireless control kit includes a transmitter and a receiver. DEVO 10 (WALKERA, Guangzhou, China) is selected for the wireless transmitter. It can send 2.4 Ghz signals of ten channels to the Pixhawk. Compared to 5 Ghz wireless signal that is also widely used in wireless signal transmission, 2.4 Ghz signal has better anti-interference performances, which makes it possible for the wireless signal transmitted as far as 20 m. Wireless transmitter has 6 channel that is used for QRA control. Wireless channels 1-4 are used to control throttle, roll, pitch and yaw of the QRA. Wireless channel 5 controls the flight modes (taking off, landing, altitude hold, loiter, etc.). To avoid unnecessary vibration of each arm caused by the arm's rotation during flight, a trigger is applied to the rotation of arms. Wireless channel 6 is used for releasing or holding the rotation of arms as a trigger. The receiver also couples with the transmitter and it is directly powered by the flight controller - Pixhawk. Like servo motor control, the signal that is transmitted from the transmitter to the receiver is PWM signal.

An external IMU sensor is also equipped with the optical flow sensor. The IMUs data from the Pixhawk and the optical flow sensor in one of the experiment is presented in Figure 3.13, where IMU1 represents IMU of Pixhawk while IMU2 represents IMU of the optical flow sensor. It can be observed that both IMU data match each other, which represents both IMU sensors work normally.

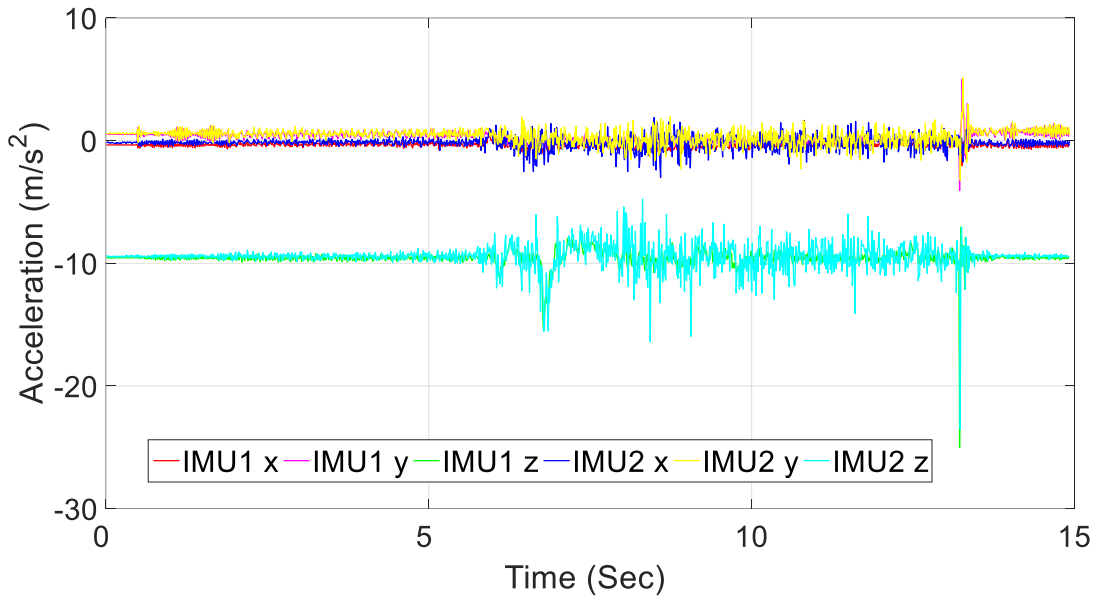


Figure 3.13 IMU data of Pixhawk and optical flow sensor

Two external sensors shown in Figure 3.14 are applied to assist flight position control during the QRA experiment. One is the optical flow sensor, which is necessary for localizing a QRA to hover at a place where is no GPS signal. By processing the image differences, the optical flow sensor can help the QRA localize itself (Honegger, et. al, 2013). This sensor has a native resolution of 752×480 pixels and a 168 MHz CPU, which makes the sensor refresh the collected data at 400 Hz with great light sensitivity.

Another external sensor is the LV-MaxSonar-EZ4 ultrasonic analog rangefinder that is installed to precisely measure the altitude that is below to 645 cm. This sensor talks to the Pixhawk through I2C port. Using these two sensors, the QRA can be anchored in a specific three-dimensional space to avoid data error caused by the potential movement when carrying the eccentric payload or effected by other disturbance during flight.

This section introduced the prototype design of QRA. The weights of each component are presented in Table 3.3.

Table 3.3 Weight of each part of the QRA

Name	Model	Weight (g)
Redesigned frame	Daya 550 frame	380
Servo motors with mounts	HS-645MG	260
BLDC motors	V3508-KV580	388
Propellers	10 × 4.7	50
Flying Controller	Pixhawk	38
Battery	4 S 5800 mAh	550
Electrical Speed Control	HobbyKing 30A	152
Other parts	-	70
Payload	-	500
Total	-	2388

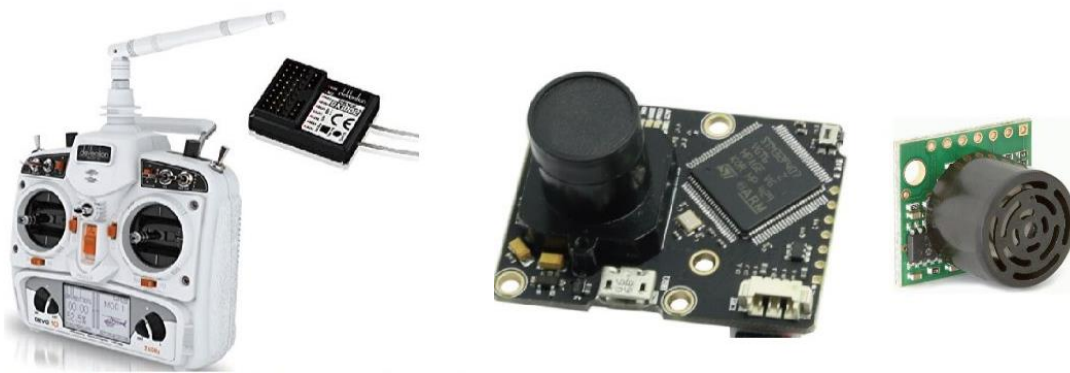


Figure 3.14 Wireless kit and external sensors (Honegger, et. al, 2013)

3.4 Control Strategy

The control system of a QRA includes a flight controller and an arm rotation controller.

The control flow chart of the QRA is presented in Figure 3.15.

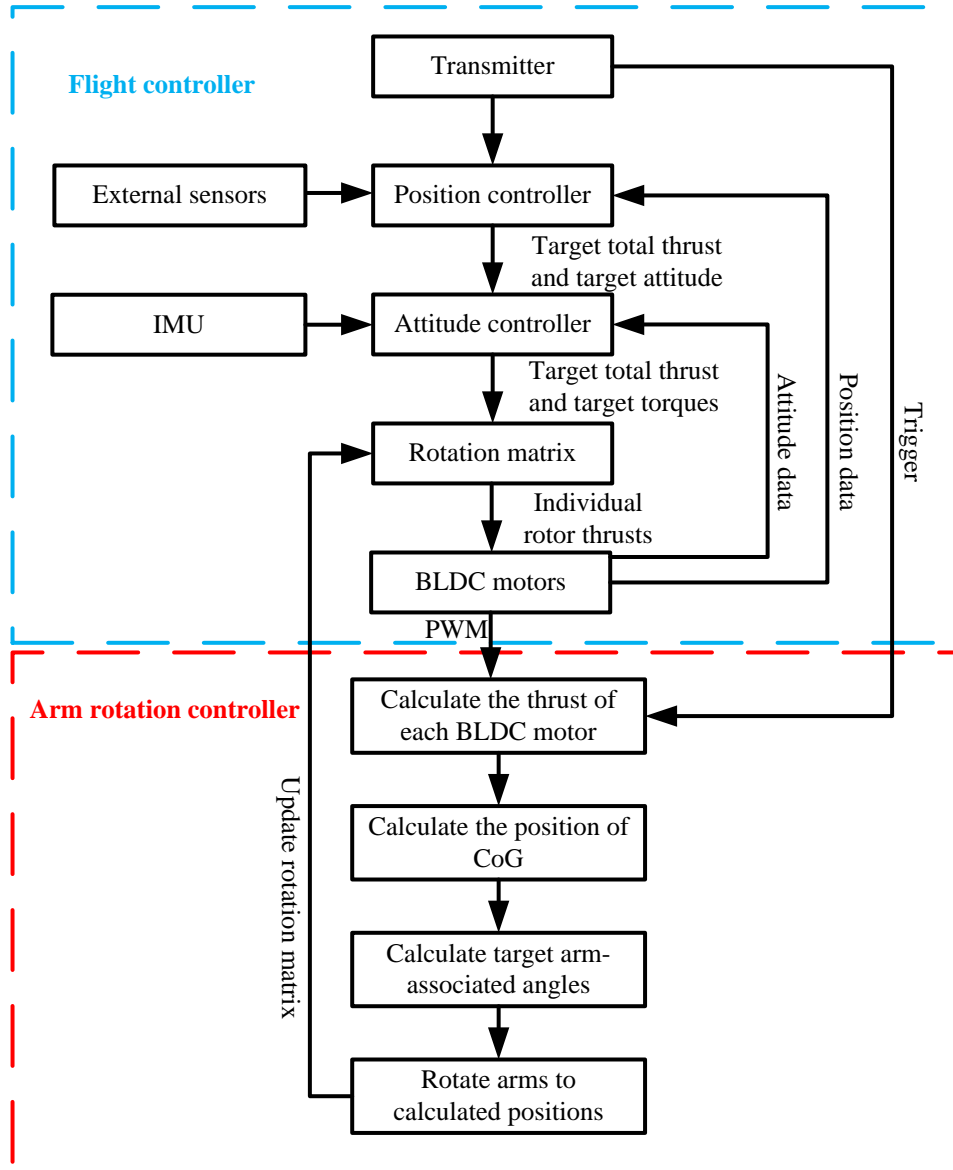


Figure 3.15 Control Strategy

3.4.1 Flight controller

Proportional-Integral-Derivative (PID) controller has been widely applied for quadrotor control (Pounds, et. al, 2012). It is robust to the dynamic changes and disturbances caused by eccentric payloads of the quadrotor (Pounds, et. al, 2012). The PID controller is applied to the

flight controller of the QRA in this study as well. A brief introduction on PID controller is made below.

For a PID controller, the term P is the proportional gain for the controller. It is the most important effect of the PID control. The P gain is proportional to the error between the current value and the desired value. If the P is much greater than an appropriate value, the controller will respond very fast but also easier to go over the target value. While term I is the integral gain of the controller. It accounts for the past for the past errors. Term I is used for diminishing the effect as the error decreases. It helps diminish the error between the current value and the desired value. For example, if only proportional gain is applied in a control system, the system value will vibrate around the desired value without diminishing the error. However, once term I is added to the control system, the average error will be diminished by time. Thus, the system can be stabilized at the desired value. The greater term I , the faster respond of the system. The term D is used for estimating the future error. If the system is changing too fast, the term D helps for dampening the effect.

The flight controller of QRA includes two PID loops, namely, attitude control loop and position control loop. The QRA keeps updating the position and attitude data and error during flight at 400 Hz (Pixhawk Autopilot). Several experiments have been done in order to get the appropriate values of PID. Table 3.4 shows the PID value that has been tested as the best value in the experiments. Figure 3.16 presents the expected and experiment value of the pitch angle control of QRA using the PID value in Table 3.4. It shows that the control is effective for the QRA.

Table 3.4 PID parameters of the QRA

Name	PID	Value
Attitude control roll	P	0.175
	I	0.150
	D	0.004
Attitude control pitch	P	0.170
	I	0.150
	D	0.003
Attitude control yaw	P	0.180
	I	0.018
	D	0.000
Throttle	P	1.000
	I	1.000
	D	0.000

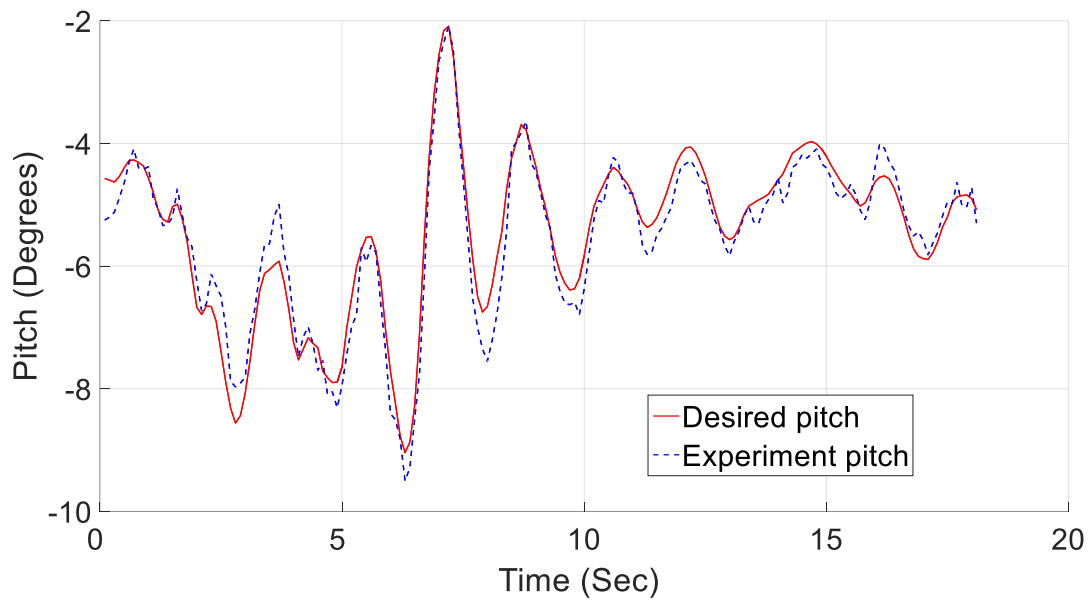


Figure 3.16 PID control experiment

The optical flow and range finder can derive the position data while IMU provides the attitude data. When the QRA is carrying an eccentric payload, its PID flight controller will initially command BLDC motors to generate different thrusts to balance the quadrotor. Then, if the arm rotation trigger of the QRA is pulled, the arm rotation controller will rotate arms of QRA to move

the symmetric center of the QRA to its CoG, taking place the difference of BLDC motor thrusts by the difference of arms of the torques generated by BLDC motor thrusts.

3.4.2 Arm rotation controller

By reading the PWM signals of each BLDC motor during flight, the arm rotation controller can calculate bias torque τ_g and target arm-associated angles to make the symmetric center back to the CoG of the QRA. The steps of implementing the arm rotation controller of the QRA are explained below.

- Check whether the trigger of the arm rotation (Channel 6 of the wireless kit) is pulled. If the PWM signal from Channel 6 is greater than 1500 us, the rotation process will be implemented, and vice versa.
- Calculate the bias torque generated by the eccentric payload. The method of calculating the bias torque is introduced in detail in subsection 3.4.2.1 below.
- Calculate the target arm-associated angles based on the current bias torque. The method of calculating the target arm-associated angles is introduced in detail in subsection 3.4.2.2 below.
- Rotate all four arms to new positions defined by the calculated target arm-associated angles.
- Update the rotation matrix of the QRA. Based on the current arm-associated angles of the QRA, the rotation matrix of the QRA can be used to transform the total thrust and torques about three axes of F_B needed to control the position and attitude in three-dimensional space to individual BLDC motor thrusts, namely,

$$\begin{bmatrix} F_1 \\ F_2 \\ F_3 \\ F_4 \end{bmatrix} = \mathbf{R} \begin{bmatrix} \tau_{rx} \\ \tau_{ry} \\ \tau_{rz} \\ F_r \end{bmatrix} \quad (15)$$

where F_r is the magnitude of the total thrust. \mathbf{R} is the rotation matrix which is defined as,

$$\mathbf{R} = \begin{bmatrix} a\sin\zeta_1 + L & a\sin\zeta_2 + L & a\sin\zeta_3 - L & a\sin\zeta_4 - L \\ a\cos\zeta_1 - W_1 & a\cos\zeta_2 + W_1 & a\cos\zeta_3 - W_2 & a\cos\zeta_4 + W_2 \\ -\frac{\tau_{d1}}{F_1} & \frac{\tau_{d2}}{F_2} & -\frac{\tau_{d3}}{F_3} & \frac{\tau_{d4}}{F_4} \\ 1 & 1 & 1 & 1 \end{bmatrix}^{-1} \quad (16)$$

3.4.2.1 Calculating the Bias Torque

The method of calculating the bias torque $\boldsymbol{\tau}_g$ and the position of the CoG \mathbf{l}_g of a QRA in hovering or in low-speed translational motion is introduced in this subsection. If the QRA is in hovering or in low-speed translational motion, the roll and the pitch of the QRA can be regarded as zero. In this case, the current bias torque could be directly obtained based on the BLDC motor thrusts. The QRA's rotation and translation dynamics equations, namely, (6) and (9), can be simplified as,

$$\boldsymbol{\tau}_r + \boldsymbol{\tau}_g = \mathbf{0} \quad (17)$$

$$\mathbf{F}_r + \mathbf{F}_g = \mathbf{0} \quad (18)$$

$\boldsymbol{\tau}_g$ can be calculated from (8) and (17) as,

$$\begin{cases} \tau_{gx} = -\tau_{rx} = -[a \sum_{i=1}^4 \cos\zeta_i F_i + L \sum_{i=1}^2 F_i - L \sum_{i=3}^4 F_i] \\ \tau_{gy} = -\tau_{ry} = -[a \sum_{i=1}^4 \sin\zeta_i F_i + W_1 \sum_{i=1}^2 (-1)^i F_i - W_2 \sum_{i=3}^4 (-1)^i F_i] \\ \tau_{gz} = -\tau_{rz} = -\sum_{i=1}^4 (-1)^i \tau_{di} = 0 \end{cases} \quad (19)$$

If the roll and the pitch of the QRA are zero, one has,

$$\mathbf{F}_g = [F_x, F_y, F_z]^T = [0, 0, -mg]^T \quad (20)$$

Substituting (19) and (20) into (7), one can calculate the l_x and l_y components of current position of the CoG in F_B as,

$$\begin{cases} l_x = \frac{1}{mg} [a \sum_{i=1}^4 \sin\zeta_i F_i + W_1 \sum_{i=1}^2 (-1)^i F_i - W_2 \sum_{i=3}^4 (-1)^i F_i] \\ l_y = -\frac{1}{mg} [a \sum_{i=1}^4 \cos\zeta_i F_i + L \sum_{i=1}^2 F_i - L \sum_{i=3}^4 F_i] \end{cases} \quad (21)$$

It should be noticed that the l_z component of the current position of the CoG cannot be obtained if a QRA is in hovering or in low-speed translational motion, because the CoG offset does not affect τ_{gz} component of the bias torque τ_g in this case.

3.4.2.2 Calculating Target Arm-Associated Angles

The method of calculating the target arm-associated angles is discussed when a QRA is in hovering or in low-speed translational motion. In order to improve the maneuvering performance and stability of the quadrotor, it is desire to have all BLDC motors of the quadrotor generate the same thrusts, rather than a difference of thrusts (Pounds, et. al, 2012; Rosen, et. al, 1989). Therefore, the target arm-associated angles, denoted by $\zeta_{ni}(i = 1,2,3,4)$, of the QRA should make the equation (17) hold with the same BLDC motor thrusts. Since τ_{gz} in the equation (19) is zero when the QRA is in hovering or in low-speed translational motion (Pounds, et. al, 2012), the equation (17) of the rotation of the QRA about z axis of F_B always holds. Then equation (17) can be simplified as,

$$\begin{cases} \tau_{gx} + [a \sum_{i=1}^4 \cos \zeta_i F_i + L \sum_{i=1}^2 F_i - L \sum_{i=3}^4 F_i] = 0 \\ \tau_{gy} - [a \sum_{i=1}^4 \sin \zeta_i F_i + W_1 \sum_{i=1}^2 (-1)^i F_i - W_2 \sum_{i=3}^4 (-1)^i F_i] = 0 \end{cases} \quad (22)$$

In order to set the symmetric center of QRA at the CoG of the QRA, in this thesis the target arm-associated angles $\zeta_{ni}(i = 1,2,3,4)$ are derived based on,

$$\begin{cases} -a \sin \zeta_{n1} + W_1 - l_x = a \sin \zeta_{n2} + W_1 + l_x \\ a \sin \zeta_{n3} + W_2 + l_x = -a \sin \zeta_{n4} + W_2 - l_x \\ a \cos \zeta_{n1} + L - l_y = -a \cos \zeta_{n4} + L + l_y \\ a \cos \zeta_{n2} + L - l_y = -a \cos \zeta_{n3} + L + l_y \end{cases} \quad (23)$$

where l_x and l_y are calculated based on the equation (21). It is also important to point out that if the target associated angle of the QRA in hovering or in low-speed translational motion make the equation (17) hold with the same BLDC motor thrusts, one has $F_i = 0.25mg(i = 1,2,3,4)$. In this

case, substituting 1) target arm-associated angles $\zeta_{ni}(i = 1,2,3,4)$ derived based on the equation (23), and 2) F_i into the equation (22), one can get,

$$\begin{cases} \tau_{gx} - mgl_y = 0 \\ \tau_{gy} + mgl_x = 0 \end{cases} \quad (24)$$

One can find that the equation (24) holds according to the equation (7), if the QRA is in hovering or in low-speed translational motion. Namely, the arm rotation controller can make all BLDC motor thrusts the same with the target arm-associated angles $\zeta_{ni}(i = 1,2,3,4)$ derived based on the equation (23), when the QRA is in hovering or in low-speed translational motion.

3.5 Summary

This chapter introduced modelling of the QRA, thrust distribution optimization for energy efficiency, prototype design, and control strategy of the QRA. It also showed the theoretical basis of the QRA. The next chapter will introduce the experiments in validation of the QRA.

CHAPTER 4. RESULTS

In this chapter, the experiments designed for energy consumption, mapping from PWM signals to thrust and from thrust to power consumption of the propulsion system of QRA are firstly introduced. After that, experiments of validation of QRA control and energy consumption of the QRA are proposed.

The platform of experiments on propulsion system is introduced below. The experiment platform is composed of Turnigy V3508-KV580 BLDC motors (FLYSKY, Shenzhen, China), HobbyKing 30 A BlueSeries (FLYSKY, Shenzhen, China), 5800 mA·h 40 c Lipo battery, and a six degrees of freedom force and torque (F/T) sensor (ATI, US) equipped on a KUKA robotic arm, as shown in Figure 4.1. The user's interface of F/T sensor is shown in Figure 4.2. The F/T sensor talks to the PC through the Ethernet. Thus, the corresponding thrust values of experiments can be read directly from the interface.

For the experiments on propulsion system, PWM signals are set to vary within 1180 us to 1800 us over the time and the corresponding, voltage and current of the battery are measured. Both 10×4.7 and 11×4.7 carbon fiber propellers are applied in the experiments to test the propulsion system performances in both situations. All experiments data on propulsion system is presented in Table 4.1 and Table 4.2.

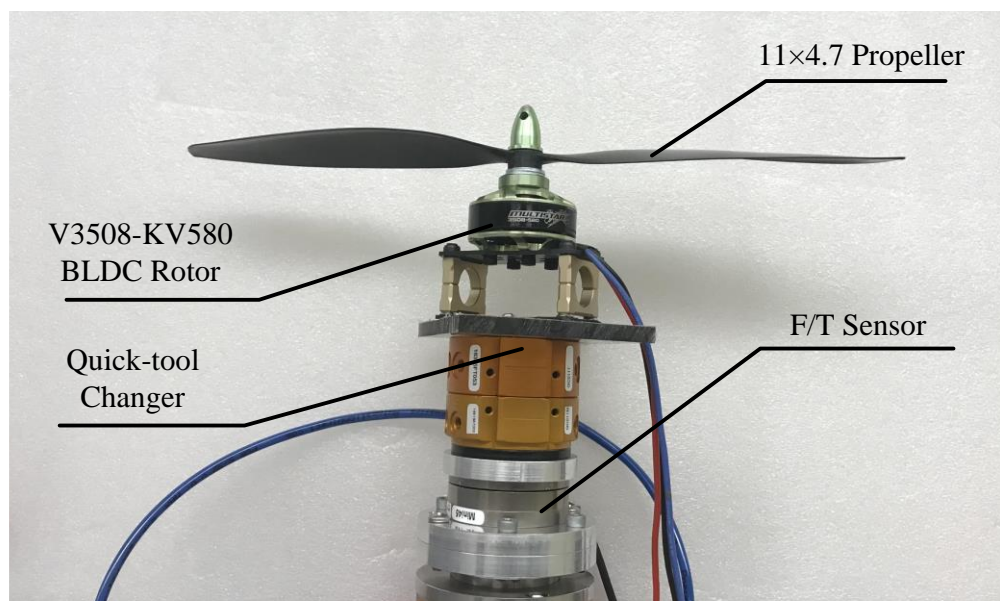


Figure 4.1 BLDC motor testing platform

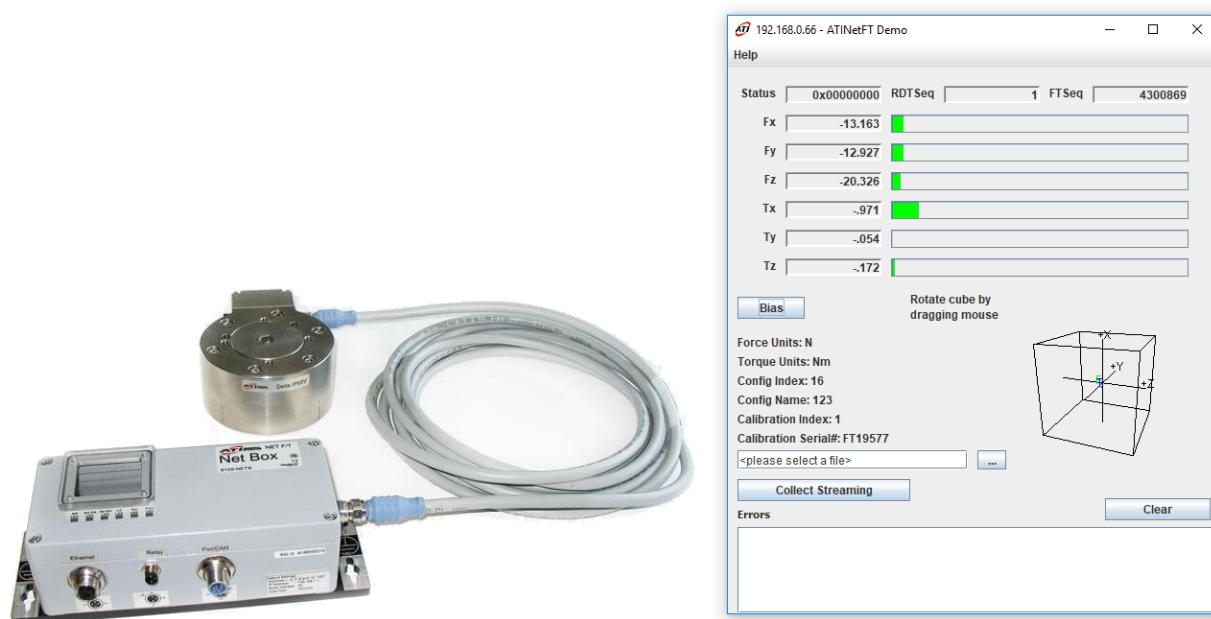


Figure 4.2 F/T sensor and user's interface ("ATI Industrial Automation", n.d.)

Table 4.1 Experiments with 10×4.7 propeller

Thrust	PWM	Voltage	Current	Power
0.29	1194	15.52	0.05	0.776
0.75	1247	15.48	0.1	1.548
1.36	1310	15.46	0.31	4.7926
1.87	1361	15.4	0.64	9.856
2.48	1400	15.39	1	15.39
3.16	1443	15.36	1.51	23.1936
3.95	1490	15.25	2.26	34.465
5.07	1540	15.13	3.31	50.0803
6.03	1582	15.05	4.28	64.414
6.95	1623	14.91	5.26	78.4266
7.76	1662	14.73	6.3	92.799
8.37	1684	14.75	7.13	105.1675
8.84	1712	14.56	7.82	113.8592
9.98	1756	14.44	9.67	139.6348
11.17	1797	14.23	11.21	159.5183

Table 4.2 Experiments with 11×4.7 propeller

Thrust	PWM	Voltage	Current	Power
1.32	1309	16.03	0.28	4.4884
1.74	1345	15.4	0.46	7.084
2.08	1378	15.97	0.75	11.9775
2.58	1424	15.91	1.09	17.3419
2.85	1451	15.35	1.27	19.4945
3.37	1480	15.81	1.7	26.877
3.95	1513	15.75	2.25	35.4375
4.55	1556	15.68	2.85	44.688
4.97	1575	15.15	3.1	46.965
5.67	1600	15.54	3.8	59.052
6.08	1628	15.11	4.34	65.5774
6.18	1652	15.33	5.11	78.3363
7.05	1681	14.98	5.61	84.0378
8.46	1729	15.09	7.21	108.7989
10.23	1794	14.84	9.4	139.496

4.1 Mapping from PWM signals to thrust of the BLDC motor

According to the arm rotation controller proposed in section 3.4, thrusts generated by the BLDC motors are the power source of the control system. The thrust of each BLDC motor is given by the equation (5). However, it's not easy to get the rotation speed of each BLDC motor in real-time. Adding additional sensors can get the thrust of every BLDC motor directly, which, however, may complicate the whole system and consume extra energy. Instead, by reading the PWM signal, the controller can get the corresponding thrust of each BLDC motor. For BLDC motors, PWM signal is not linearly proportional to the thrust because of the energy losses. Therefore, a curve fitting has been done to map from PWM signals to thrust of the BLDC motor.

A third-order curve is applied to the mapping. Let d denotes the PWM value, the thrust is given by,

$$T = -1.554 \times 10^{-8}d^3 + 8.689 \times 10^{-5}d^2 - 0.1364d + 65.78 \quad (26)$$

Figure 4.3 shows the PWM signals and thrust values from the experiment and the fitted curve.

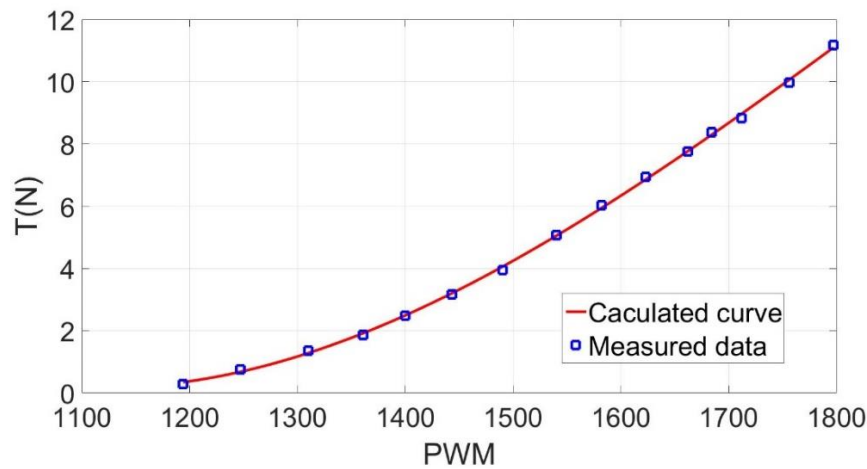


Figure 4.3 PWM versus thrust of BLDC motor

4.2 Mapping from the thrust to the power consumption of BLDC motor

The power consumption of QRA is computed as the product of voltage of the battery and current. However, the thrust generated by the BLDC motor is also not linear to the power consumption. For the same propeller, the BLDC motor efficiency would decrease as the rotation speed increases. The faster the BLDC motor rotates, the larger current is needed, resulting in heat and mechanical losses. In order to get the calculated power consumption, an experiment is designed to map the thrust to the power of BLDC motor.

For the BLDC motor, it has been proposed that the power consumption is a function of thrust (Atlam & Kolhe, 2013),

$$P_r = f(F) = K_p F^{1.5} \quad (18)$$

where P_r is the power consumption of the BLDC motor, F is the generated thrust, and K_p is a motor and propeller-dependent coefficient.

The mathematical model matches the measured data in the experiment. Figure 4.4 shows the calculated matching curve and the estimated curve of the thrust versus power consumption for the BLDC motor.

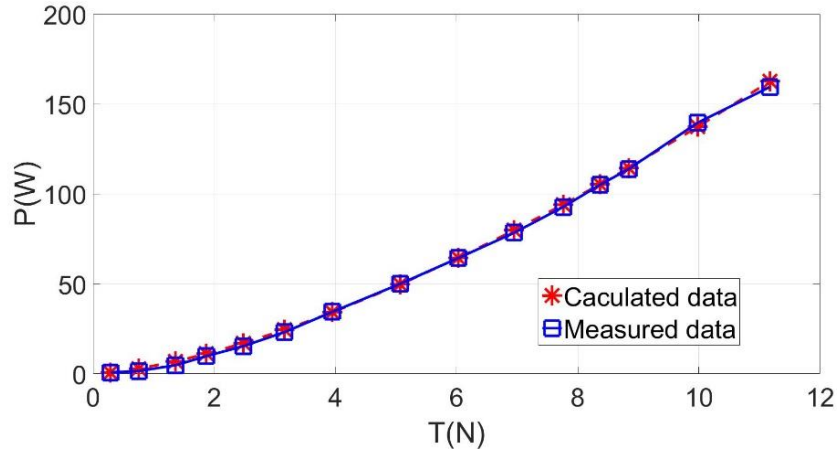


Figure 4.4 Thrust versus the power of BLDC motor

4.3 Validation of the Arm Rotation Control (ARC)

The QRA has been tested in two experiments to validate its performance of stability and energy efficiency. The only difference in two experiments is the location of the payload to the QRA. For each experiment, I compare the experiment and calculated data from the QRA during hovering. Figure 4.5 shows the field experiment where has light breezes.

The quadrotor is commanded to loiter where the altitude is 1.5 m with a payload of 500 g for both experiments. Figures 4.6 and 4.7 show the calculated and experiment outputs of four BLDC motors in two experiments. The details of each experiment are given below. Table 4.3 shows the parameters of QRA in the experiments. Appropriate attitude control (Roll, Pitch, and Yaw) PID values shown in Table 3.4 were acquired from preliminary tests of QRA.

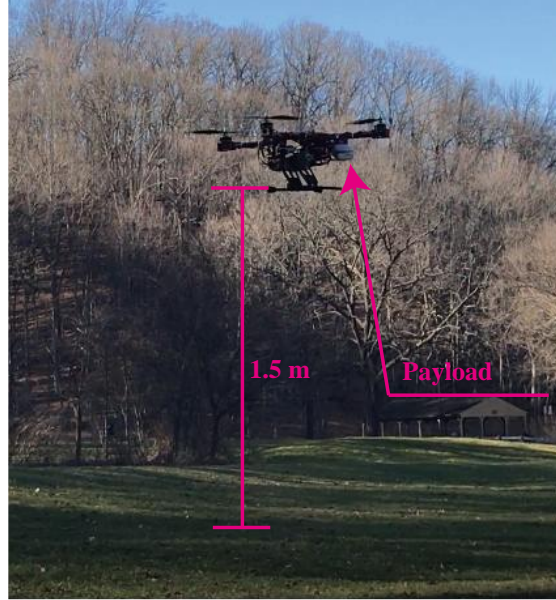


Figure 4.5 Field experiments

Table 4.3 Parameters of the QRA in the experiment

Parameters	Value
g	9.8 m/s^2
L	0.048 m
$W1$	0.020 m
$W2$	0.053 m
ζ_{ni}	$25^\circ - 65^\circ$

In the first experiment, the payload is placed on the origin of the F_B of the QRA and four arms of the QRA are not allowed to rotate. In other words, the QRA in this experiment is actually a conventional QFA. Since the payload position in this experiment does not cause the displacement of CoG for the QRA, the bias torque is zero. Therefore, the outputs of the four BLDC motors should be identical, according to the dynamics model developed in section 3.1 dynamics modeling. The weight of the quadrotor with the payload as a whole is 2,388 g, which means each BLDC motor needs to provide a thrust of 5.85 N. A thrust of 5.85 N maps to a PWM value of 1,578 in the calculation. Figure 4.6 shows the mean values of outputs for i th BLDC motor ($i=1,2,3,4$)

during hovering are 1,581, 1,587, 1,580, and 1,588, respectively. The naming convention of the BLDC motors follows the rules in Figure 3.2. Experiment results agree with the calculated results when the payload is at the symmetric center of the quadrotor.

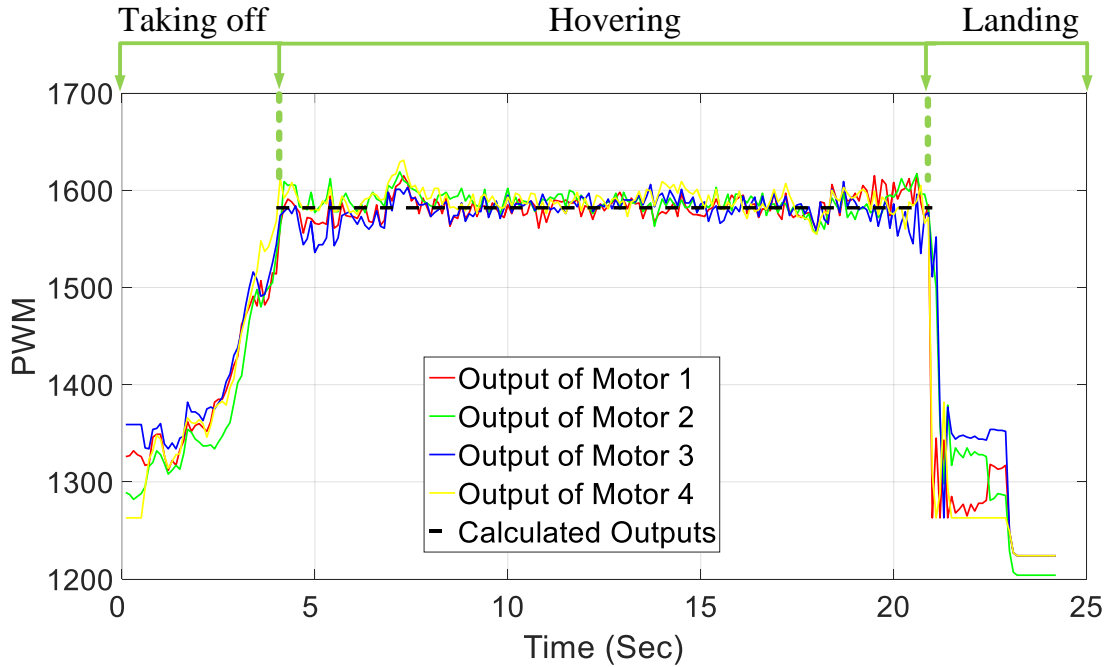


Figure 4.6 Outputs when hovering with the payload at the symmetric center of quadrotor

In the second experiment, the quadrotor carries a payload of 500 g at (0, 19 cm, 0) of F_B . The CoG position of the quadrotor is manually measured at (0, 3.6 cm, 0) of F_B . Figure 4.6 shows the outputs of four BLDC motors of quadrotor at hovering during this experiment.

After taking off, for the first 66 seconds I keep four arms fixed like a QFA at hovering with the eccentric load. Then, the ARC is enabled. As shown in Figure 4.7, It can be seen that not only the hovering stability but also the thrust distribution benefit from the ARC.

For the stability, when the quadrotor with fixed arms taking an eccentric payload, the PWM outputs changes significantly to keep the desired attitude. The amplitudes of four outputs are obviously greater than those after the ARC. Standard variation of PWM outputs of each BLDC motor is reduced from (26.21, 31.44, 27.48, 29.62) to (11.02, 12.15, 11.76, 8.88) due to the ARC.

For the thrust distribution. The experiment results also match the calculated ones well. Before the operation of the ARC, the PWM output curves of BLDC motor 1 and BLDC motor 3 are above the curves of BLDC motor 2 and BLDC motor 4 (Figure 4.7). Because of the displacement of the CoG, to keep the balance of quadrotor at hovering, two BLDC motors in the heavier side (motors 1 and 3) need to produce greater thrusts than motors 2 and 4 to compensate the bias torque caused by the displacement of the CoG. After the operation of the ARC, the mean values of outputs are reduced from 1621 to 1586 for BLDC motor 1, and 1586 to 1573 for BLDC motor 3, while the mean values of outputs are increased from 1547 to 1569 for BLDC motor 2, and 1554 to 1563 for BLDC motor 4. For the calculation, before the ARC, the calculated outputs for BLDC motor 1 and 3 is 1634, and 1529 for BLDC motor 2 and 4. After the ARC, the calculated outputs of all motors are 1578. Experiment results that are shown in Table 4.4 match the calculated values when the payload is at the symmetric center of the quadrotor.

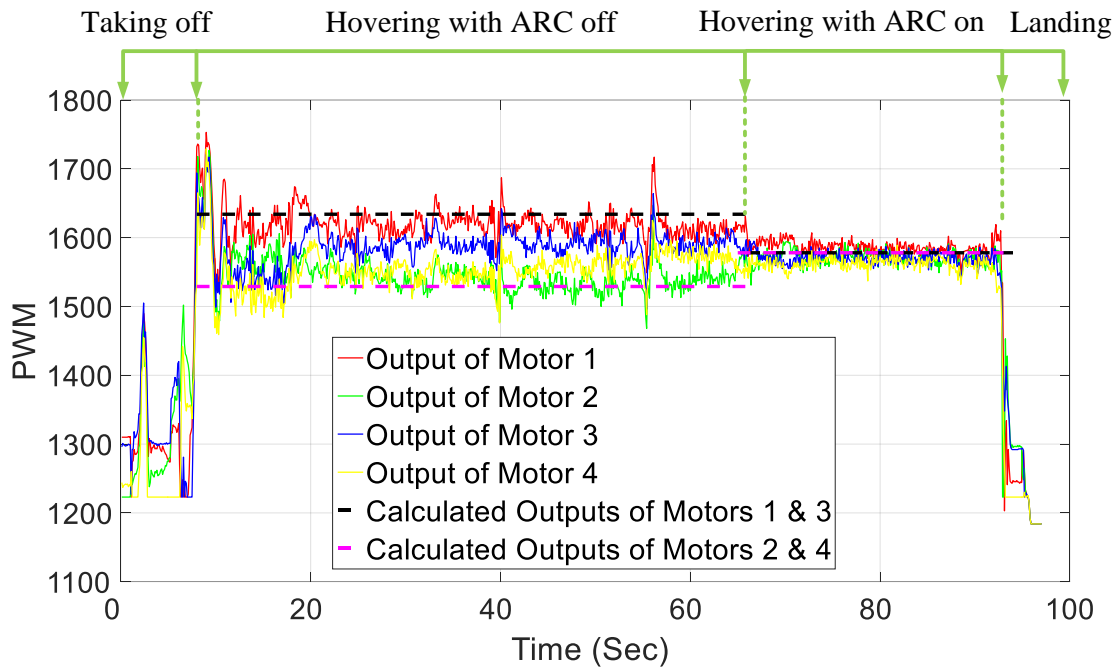


Figure 4.7 Outputs when hovering with the eccentric payload

Table 4.4 Experiment results when the QRA hovering with the eccentric payload

	Mean values of PWM		Standard deviation of PWM	
	ARC OFF	ARC ON	ARC OFF	ARC ON
Motor 1	1,621	1,586	26.21	11.02
Motor 2	1,547	1,569	31.44	12.15
Motor 3	1,586	1,573	27.48	11.76
Motor 4	1,554	1,563	29.62	8.88

4.4 Energy Consumption

The voltage of the battery and current are recorded by the power module in the second experiment to validate the energy consumption performance for the QRA. The power values in Figure 4.8 are the product of the current and voltage of the battery measured by the power module.

After ARC, the power consumption reduces from 259.6 W to 249.4 W, the power consumption reduces 3.93% after the ARC in the second experiment. For the calculation in an ideal situation, the power reduced from 260.6 W to 250.2 W, which reduces 3.99%. The experiment value also matches the calculated one.

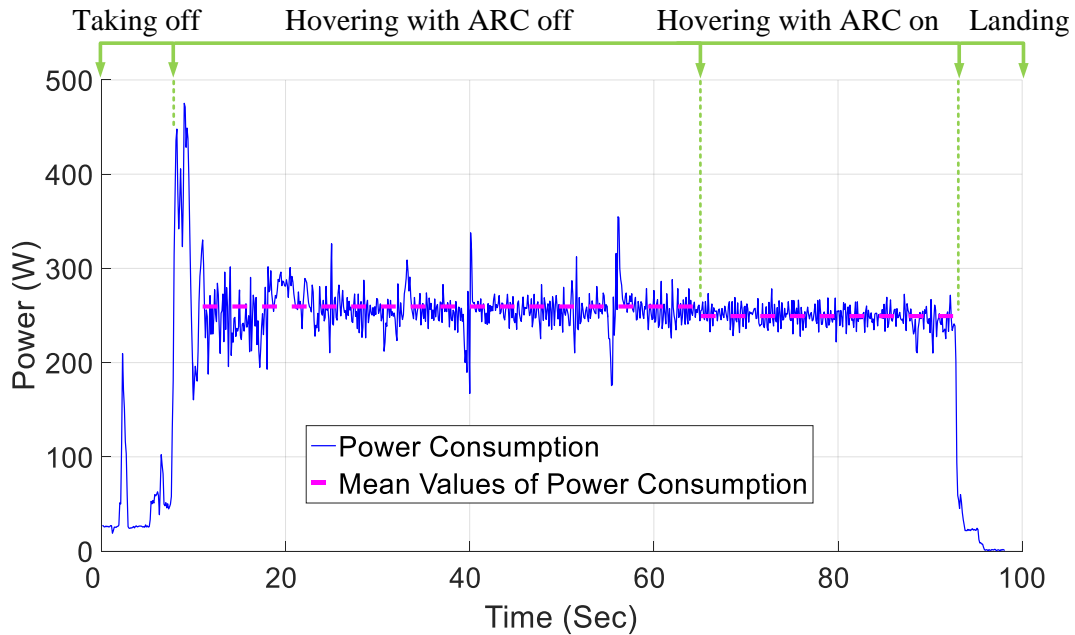


Figure 4.8 Power consumption

4.5 Summary

This chapter introduced the experiments designed for energy consumption, mapping from PWM signals to thrust and from thrust to power consumption of the propulsion system of the QRA, and experiments of validation of the QRA control and energy consumption of the QRA. This chapter validated the control strategy of the QRA and presented the QRA has better flying performance of stability and energy consumption than the QFA.

CHAPTER 5. SUMMARY, CONCLUSIONS, AND RECOMMENDATIONS

The conclusions and recommendations regarding the design, modeling, and control of a quadrotor with rotatable arms are discussed in this chapter.

5.1 Conclusions

This thesis explores a QRA that can automatically compensate the eccentric payload to increase the stability and energy efficiency. The thesis presents the dynamics modeling and control strategy for the QRA. The thesis also introduces detailed prototype design of QRA. Experiments have been done to validate the algorithm and the performance of the QRA. The experiment results are compared to the calculated values, which validates the arm rotation control of the QRA. Through the experiment results, the thesis demonstrates the QRA has better flying performance of stability and energy efficiency than a QFA with the same arms, weight, BLDC motors, and eccentric payloads. The QRA provides a solution that can move the symmetric center of the quadrotor at the location of its CoG when carrying an eccentric payload.

5.2 Recommendations

QRA has meaningful applications in aerial manipulation. The flying performance is interesting to see when install a robotic arm or cradle head on the QRA, instead of using a fixed eccentric payload, to mimic real aerial manipulation. For the applications in aerial delivery, I also plan to conduct more experiments with arm rotation control when the QRA is flying. Different arm-associated angles would also influence the flying performance.

LIST OF REFERENCES

- Alaimo, A., Artale, V., Milazzo, C., Ricciardello, A., & Trefiletti, L. (2013, May). Mathematical modeling and control of a hexacopter. In *Unmanned Aircraft Systems (ICUAS), 2013 International Conference on* (pp. 1043-1050). IEEE.
- Alibaba Group. (n.d.). Retrieved April 20, 2018, from <https://www.aliexpress.com/item/DAYA-550-550mm-Alien-Carbon-Fiber-Folding-4-Axis-FPV-Quadcopter-Frame-Kit/2047249054.html>
- Amazon Prime Air. (n.d.). Retrieved November 14, 2017, from <https://www.amazon.com/b?node=8037720011>
- Amin, R., Saeid, T., Masoud, N., Hossein, S., Majid, S & Amin, M,. (2013). Robotics Tomorrow. Retrieved April 20, 2018, from http://www.roboticstomorrow.com/content.php?post_type=1912ty
- Antonelli, G., Cataldi, E., Giordano, P. R., Chiaverini, S., & Franchi, A. (2013, November). Experimental validation of a new adaptive control scheme for quadrotors MAVs. In *Intelligent Robots and Systems (IROS), 2013 IEEE/RSJ International Conference on* (pp. 2439-2444). IEEE.
- Ariyanto, M., & Naniwa, T. (2016, October). Mathematical and physical modelling with dynamic change in the center of gravity of quadrotor. In *Information Technology and Electrical Engineering (ICITEE), 2016 8th International Conference on* (pp. 1-6). IEEE.
- ArduPilot Autopilot Suite. (2016). Retrieved November 26, 2017, from <http://ardupilot.org/ardupilot/>
- ATI Industrial Automation. (n.d.). Net F/T. Retrieved November 14, 2017, from http://www.ati-ia.com/products/ft/ft_NetFT.aspx
- Atlam, O., & Kolhe, M. (2013). Performance evaluation of directly photovoltaic powered DC PM (direct current permanent magnet) motor–propeller thrust system. *Energy*, 57, 692-698.
- Bartelds, T., Capra, A., Hamaza, S., Stramigioli, S., & Fumagalli, M. (2016). Compliant aerial manipulators: Toward a new generation of aerial robotic workers. *IEEE Robotics and Automation Letters*, 1(1), 477-483.
- Basri, M. A. M., Husain, A. R., & Danapalasingam, K. A. (2015). Enhanced backstepping controller design with application to autonomous quadrotor unmanned aerial vehicle. *Journal of Intelligent & Robotic Systems*, 79(2), 295-321.

- Benito, J. A., Glez-de-Rivera, G., Garrido, J., & Ponticelli, R. (2014, November). Design considerations of a small UAV platform carrying medium payloads. In *Design of Circuits and Integrated Circuits (DCIS), 2014 Conference on* (pp. 1-6). IEEE.
- Bergamasco, M., & Lovera, M. (2014). Identification of linear models for the dynamics of a hovering quadrotor. *IEEE Transactions on Control Systems Technology*, 22(5), 1696-1707.
- Bouadi, H., Cunha, S. S., Drouin, A., & Mora-Camino, F. (2011, November). Adaptive sliding mode control for quadrotor attitude stabilization and altitude tracking. In *Computational Intelligence and Informatics (CINTI), 2011 IEEE 12th International Symposium on* (pp. 449-455). IEEE.
- Brandt, J. B. (2005). Small-scale propeller performance at low speeds (Doctoral dissertation, University of Illinois at Urbana-Champaign).
- Bristeau, P. J., Martin, P., Salaün, E., & Petit, N. (2009, August). The role of propeller aerodynamics in the model of a quadrotor UAV. In *Control Conference (ECC), 2009 European* (pp. 683-688). IEEE.
- Cheung, Z., Delizo, M.Z. (1998). Confined Space Guide, *California Dept. of Education*.
- Choi, Y. C., & Ahn, H. S. (2015). Nonlinear control of quadrotor for point tracking: Actual implementation and experimental tests. *IEEE/ASME transactions on mechatronics*, 20(3), 1179-1192.
- Choi, I. H., & Bang, H. C. (2012). Adaptive command filtered backstepping tracking controller design for quadrotor unmanned aerial vehicle. Proceedings of the Institution of Mechanical Engineers, Part G: *Journal of Aerospace Engineering*, 226(5), 483-497.
- Chovancová, A., Fico, T., Chovanec, L., & Hubinsk, P. (2014). Mathematical modelling and parameter identification of quadrotor (a survey). *Procedia Engineering*, 96, 172-181.
- Das, A., Lewis, F., & Subbarao, K. (2009). Backstepping approach for controlling a quadrotor using lagrange form dynamics. *Journal of Intelligent and Robotic Systems*, 56(1-2), 127-151.
- Derafa, L., Madani, T., & Benallegue, A. (2006, December). Dynamic modelling and experimental identification of four rotors helicopter parameters. In *Industrial Technology, 2006. ICIT 2006. IEEE International Conference on* (pp. 1834-1839). IEEE.
- Dickson, J., Kulinka, C., Martin, M., Yeol, J., & Clark, J. (2011). Development and Integration of Adaptive Robotic Multi-Modal System. *Aerospace Sciences Meeting including the New Horizons Forum and Aerospace Exposition*. doi:10.2514/6.2011-1283

- Dogger, J. D., Roossien, B., & Nieuwenhout, F. D. (2011). Characterization of Li-ion batteries for intelligent management of distributed grid-connected storage. *IEEE Transactions on Energy Conversion*, 26(1), 256-263.
- Doyle, C. E., Bird, J. J., Isom, T. A., Kallman, J. C., Bareiss, D. F., Dunlop, D. J. & Minor, M. A. (2013). An Avian-Inspired Passive Mechanism for Quadrotor Perching. *Transactions on Mechatronics*, 18(2), 506-517. doi:10.1109/tmech.2012.2211081
- Dydek, Z. T., Annaswamy, A. M., & Lavretsky, E. (2013). Adaptive control of quadrotor UAVs: A design trade study with flight evaluations. *IEEE Transactions on control systems technology*, 21(4), 1400-1406.
- Efe, M. Ö. (2011). Integral sliding mode control of a quadrotor with fractional order reaching dynamics. *Transactions of the Institute of Measurement and Control*, 33(8), 985-1003.
- Fumagalli, M., Naldi, R., Macchelli, A., Forte, F., Keemink, A. Q., Stramigioli, S., ... & Marconi, L. (2014). Developing an aerial manipulator prototype: Physical interaction with the environment. *IEEE robotics & automation magazine*, 21(3), 41-50.
- Fumagalli, M., & Carloni, R. (2013, November). A modified impedance control for physical interaction of UAVs. In *Intelligent Robots and Systems (IROS), 2013 IEEE/RSJ International Conference on* (pp. 1979-1984). IEEE.
- Haus, T., Orsag, M., & Bogdan, S. (2017). Mathematical Modelling and Control of an Unmanned Aerial Vehicle with Moving Mass Control Concept. *Journal of Intelligent & Robotic Systems*, 88(2-4), 219-246.
- Heredia, G., Jimenez-Cano, A. E., Sanchez, I., Llorente, D., Vega, V., Braga, J., ... & Ollero, A. (2014, September). Control of a multirotor outdoor aerial manipulator. In *Intelligent Robots and Systems (IROS 2014), 2014 IEEE/RSJ International Conference on* (pp. 3417-3422). IEEE.
- Hoffmann, G., Rajnarayan, D., Waslander, S., Dostal, D., Jang, J., & Tomlin, C. (2004). The Stanford testbed of autonomous rotorcraft for multi agent control (STARMAC). *The 23rd Digital Avionics Systems Conference* (IEEE Cat. No.04CH37576). doi:10.1109/dasc.2004.1390847
- Honegger, D., Meier, L., Tanskanen, P., & Pollefeys, M. (2013, May). An open source and open hardware embedded metric optical flow cmos camera for indoor and outdoor applications. In *Robotics and Automation (ICRA), 2013 IEEE International Conference on* (pp. 1736-1741). IEEE.
- Honglei, A., Jie, L., Jian, W., Jianwen, W., & Hongxu, M. (2013). Backstepping-based inverse optimal attitude control of quadrotor. *International Journal of Advanced Robotic Systems*, 10(5), 223.

- Hu, J, Liang, Y, & Diao, X. (2017) A Flying-Insect-Inspired Hybrid Robot for Disaster Exploration. *2017 IEEE International Conference on Robotics and Biomimetics (ROBIO)*.
- Kalantari, A., & Spenko, M. (2014). Modeling and Performance Assessment of the HyTAQ, a Hybrid Terrestrial/Aerial Quadrotor. *IEEE Transactions on Robotics*, 30(5), 1278-1285. doi:10.1109/tro.2014.2337555
- Kemper, M., & Fatikow, S. (2006). Impact of center of gravity in quadrotor helicopter controller design. *IFAC Proceedings Volumes*, 39(16), 157-162.
- Kessens, C. C., Young, A., Fearing, R. S., & Full, R. J. (2016). Cockroach-inspired winged robot reveals principles of ground-based dynamic self-righting. *International Conference on Intelligent Robots and Systems*. doi:10.1109/iros.2016.7759334.
- Kim, S., Choi, S., & Kim, H. J. (2013, November). Aerial manipulation using a quadrotor with a two dof robotic arm. In *Intelligent Robots and Systems (IROS), 2013 IEEE/RSJ International Conference on* (pp. 4990-4995). IEEE.
- Korpela, C., Orsag, M., Danko, T., Kobe, B., McNeil, C., Pisch, R., & Oh, P. (2012, May). Flight stability in aerial redundant manipulators. In *Robotics and Automation (ICRA), 2012 IEEE International Conference on* (pp. 3529-3530). IEEE.
- Kumar, V., & Michael, N. (2012). Opportunities and challenges with autonomous micro aerial vehicles. *The International Journal of Robotics Research*, 31(11), 1279-1291.
- Kushleyev, A., Kumar, V., & Mellinger, D. (2012). Towards A Swarm of Agile Micro Quadrotors. *Robotics: Science and Systems VIII*. doi:10.15607/rss.2012.viii.028
- Luukkonen, T. (2011). Modelling and control of quadrotor. Independent research project in *applied mathematics*, Espoo.
- Lee, J. Y., Cook, Z., Barzilov, A., & Yim, W. (2016, November). Control of an aerial manipulator with an on-board balancing mechanism. In *ASME 2016 International Mechanical Engineering Congress and Exposition* (pp. V04AT05A019-V04AT05A019). American Society of Mechanical Engineers.
- Lee, T. (2016). Retrieved April 20, 2018, from <https://www.techinasia.com/dhl-ecommerce-logistics-southeast-asia>
- Madani, T., & Benallegue, A. (2006, December). Control of a quadrotor mini-helicopter via full state backstepping technique. In *Decision and Control, 2006 45th IEEE Conference on* (pp. 1515-1520). IEEE.
- Mahony, R., Kumar, V., & Corke, P. (2012). Multirotor aerial vehicles: Modeling, estimation, and control of quadrotor. *Robotics Automation Magazine*, 19, 20-32.

- Mayhew et al. C. Mayhew, R. Sanfelice, and A. Teel. On path-lifting mechanisms and unwinding in quaternion-based attitude control. *Automatic Control*, IEEE Transactions on. PP (99), 1-1.
- Mellinger, D., Lindsey, Q., Shomin, M., & Kumar, V. (2011, September). Design, modeling, estimation and control for aerial grasping and manipulation. In *Intelligent Robots and Systems (IROS), 2011 IEEE/RSJ International Conference on* (pp. 2668-2673). IEEE.
- Michael, N., Fink, J., & Kumar, V. (2011). Cooperative manipulation and transportation with aerial robots. *Autonomous Robots*, 30(1), 73-86.
- Mohd Basri, M. A., Husain, A. R., & Danapalasingam, K. A. (2015). Intelligent adaptive backstepping control for MIMO uncertain non-linear quadrotor helicopter systems. *Transactions of the Institute of Measurement and Control*, 37(3), 345-361.
- Mahony, R., Kumar, V., & Corke, P. (2012). Multirotor aerial vehicles: Modeling, estimation, and control of quadrotor. *Robotics Automation Magazine*, 19, 20-32.
- Nicol, C., Macnab, C. J. B., & Ramirez-Serrano, A. (2011). Robust adaptive control of a quadrotor helicopter. *Mechatronics*, 21(6), 927-938.
- Orsag, M., Korpela, C. M., Bogdan, S., & Oh, P. Y. (2014). Hybrid adaptive control for aerial manipulation. *Journal of intelligent & robotic systems*, 73(1-4), 693.
- Palunko, I., Fierro, R., & Cruz, P. (2012, May). Trajectory generation for swing-free maneuvers of a quadrotor with suspended payload: A dynamic programming approach. In *Robotics and Automation (ICRA), 2012 IEEE International Conference on* (pp. 2691-2697). IEEE.
- Piccoli, M., & Yim, M. (2014, May). Passive stability of a single actuator micro aerial vehicle. In *Robotics and Automation (ICRA), 2014 IEEE International Conference on* (pp. 5510-5515). IEEE.
- Piccoli, M., Revzen, S., & Yim, M. (2013). SEAL Pack versatile, portable, and rapidly deployable SEa, air, and land vehicle. *International Symposium on Safety, Security, and Rescue Robotics*. doi:10.1109/ssrr.2013.6719362
- Pixhawk Autopilot. (n.d.). Retrieved November 26, 2017, from <https://pixhawk.org/modules/pixhawk>
- Pope, M. T., Kimes, C. W., Jiang, H., Hawkes, E. W., Estrada, M. A., Kerst, C. F. & Cutkosky, M. R. (2017). A Multimodal Robot for Perching and Climbing on Vertical Outdoor Surfaces. *Transactions on Robotics*, 33(1), 38-48. doi:10.1109/tro.2016.2623346
- Pounds, P., Mahony, R., & Corke, P. (2010). Modelling and control of a large quadrotor robot. *Control Engineering Practice*, 18(7), 691-699.

- Pounds, P. E., Bersak, D. R., & Dollar, A. M. (2012). Stability of small-scale UAV helicopters and quadrotors with added payload mass under PID control. *Autonomous Robots*, 33(1-2), 129-142.
- Pounds, P. E., Mahony, R. E., & Corke, P. I. (2009). Design of a Static Thruster for Microair Vehicle Rotorcraft. *Journal of Aerospace Engineering*, 22(1), 85-94. doi:10.1061/(asce)0893-1321(2009)22:1(85)
- Quan, Q. (2017). *Introduction to Multicopter Design and Control*. Springer.
- Radiolink PixHawk Advanced Autopilot. (n.d.). Retrieved April 20, 2018, from <https://www.robotshop.com/en/radiolink-pixhawk-advanced-autopilot.html>
- Rinaldi, F., Chiesa, S., & Quagliotti, F. (2013). Linear quadratic control for quadrotors UAVs dynamics and formation flight. *Journal of Intelligent & Robotic Systems*, 70(1-4), 203-220.
- Rosen, A., Ronen, T., & Raz, R. (1989). Active aerodynamic stabilization of a helicopter/sling-load system. *Journal of Aircraft*, 26(9), 822-828.
- Rose, L. (2012). *On Math and Science*. Retrieved April 20, 2018, from <https://www.pinterest.com/pin/26810560253070861>
- Rossi, R., & Rocco, P. (2016). Trajectory Generation and Control for Aerial Manipulation. Retrieved August 25, 2017, from <http://sidra2016.dia.uniroma3.it/trajectory-generation-control-aerial-manipulation/>
- Simetti, E., & Casalino, G. (2016). A novel practical technique to integrate inequality control objectives and task transitions in priority based control. *Journal of Intelligent & Robotic Systems*, 84(1-4), 877-902.
- Turnigy Brushless Multi-Rotor Motor (n.d.). Retrieved April 20, 2018, from https://hobbyking.com/en_us/3508-380kv-turnigy-multistar-14-pole-brushless-multi-rotor-motor-with-extra-long-leads.html
- Turpin, M., Michael, N., & Kumar, V. (2012). Decentralized formation control with variable shapes for aerial robots. *International Conference on Robotics and Automation*. doi:10.1109/icra.2012.6225196
- U.S. Department of Labor. (2015). Protecting Construction Workers in Confined Spaces: *Small Entity Compliance Guide*.
- Yeong, S. P., King, L. M., & Dol, S. S. (2015). A review on marine search and rescue operations using unmanned aerial vehicles. *Int. J. Mech. Aerosp. Ind. Mech. Manuf. Eng*, 9, 396-399.

V3508-KV580 Tech Specs. (n.d.). Retrieved November 11, 2017, from <http://www.rcsunnysky.com/index.php?s=/article/detail/id/125/m/Home.html&lang=en-us>

Zheng, E. H., Xiong, J. J., & Luo, J. L. (2014). Second order sliding mode control for a quadrotor UAV. *ISA transactions*, 53(4), 1350-1356.

ZIPPY Compact 5800mAh 4s 40c Lipo Pack. (n.d.). Retrieved April 20, 2018, from https://hobbyking.com/en_us/zippy-compact-5800mah-4s-40c-lipo-pack.html

Zygmund, A. (1953). HG Hardy, JE Littlewood and G. Pólya, Inequalities. *Bulletin of the American Mathematical Society*, 59(4), 411-412.

APPENDIX A. PROGRAM CODE

```

/* Arm's Rotation Control */
void SRV_Channels::output_ch_all(void)
{
    int8_t passthrough_from = -1;
    uint16_t radio = 1100;

    passthrough_from = int8_t(56 - 51);
    RC_Channel *rc = RC_Channels::rc_channel(passthrough_from);
    if (rc) {
        if (SRV_Channels::passthrough_disabled()) {
            radio = rc->get_radio_trim();
        }
        else {
            radio = rc->get_radio_in();
        }
    }
}

/*Initialization for neutral position of servo motors when PWM is 1500*/

if (radio > 1500) {
    channels[4].theta_a.set_and_save_ifchanged((float)0);
    channels[4].theta_b.set_and_save_ifchanged((float)0);

    for (uint8_t i = 0; i < NUM_SERVO_CHANNELS; i++) {
        if (i == (uint8_t)4) {

            hal.rcout->write(channels[4].ch_num, (uint16_t)(1500));
        }
        else if (i == (uint8_t)5) {
            hal.rcout->write(channels[5].ch_num, (uint16_t)(1500));
        }
        else if (i == (uint8_t)6) {
            hal.rcout->write(channels[6].ch_num, (uint16_t)(1500));
        }
        else if (i == (uint8_t)7) {
            hal.rcout->write(channels[7].ch_num, (uint16_t)(1500));
        }
        else {
            channels[i].output_ch();
        }
    }
}
else {
    double x = (double)channels[0].get_output_pwm();
    double y = (double)channels[1].get_output_pwm();
    double z = (double)channels[2].get_output_pwm();
    double w = (double)channels[3].get_output_pwm();

    /*Arm-associated angles*/

    double T1 = (double)0.00001535 * x * x - (double) 0.03334 * x + (double) 18.23;
    double T2 = (double)0.00001535 * y * y - (double) 0.03334 * y + (double) 18.23;
    double T3 = (double)0.00001535 * z * z - (double) 0.03334 * z + (double) 18.23;

```

```

double T4 = (double)0.00001535 * w * w - (double) 0.03334 * w + (double) 18.23;

double F1 = (double)(T1 + T4);
double F2 = (double)(T2 + T3);
double a = (double) 204.381536244;
double h = (double)(F2 - F1) * a / (F2 + F1);
double theta_2 = ((double)acos(cos(0.785398) - (h / (2 * 222.5)))) -
(double)0.785398);
double theta_1 = ((double)acos(cos(0.785398) + (h / (2 * 208.5)))) -
(double)0.785398);

/* Limitations of Arm-associated angles */

if (theta_1 * 57.2958 > 30) {
    theta_1 = 30 / 57.2958;
}
else if (theta_1 * 57.2958 < -30) {
    theta_1 = -30 / 57.2958;
}

if (theta_2 * 57.2958 > 30) {
    theta_2 = 30 / 57.2958;
}
else if (theta_1 * 57.2958 < -30) {
    theta_1 = -30 / 57.2958;
}

double theta_a = 0;
double theta_b = 0;

if (channels[4].get_theta_a() == 0 && channels[4].get_theta_b() == 0)
{
    channels[4].theta_a.set_and_save_ifchanged((float)theta_1);
    channels[4].theta_b.set_and_save_ifchanged((float)theta_2);
    theta_a = theta_1;
    theta_b = theta_2;
}
else
{
    theta_a = channels[4].get_theta_a();
    theta_b = channels[4].get_theta_b();
}

/* Servo outputs for a simplified model*/

for (uint8_t i = 0; i < NUM_SERVO_CHANNELS; i++) {
    if (i == (uint8_t)4) {
        hal.rcout->write(channels[4].ch_num, (uint16_t)(1500 - 10 * theta_b *
57.2958));
    }
    else if (i == (uint8_t)5) {
        hal.rcout->write(channels[5].ch_num, (uint16_t)(1500 + 10 * theta_a *
57.2958));
    }
    else if (i == (uint8_t)6) {
        hal.rcout->write(channels[6].ch_num, (uint16_t)(1500 - 10 * theta_a *
57.2958));
    }
}

```

```
        else if (i == (uint8_t)7) {  
            hal.rcout->write(channels[7].ch_num, (uint16_t)(1500 + 10 * theta_b *  
57.2958));  
        }  
        else {  
            channels[i].output_ch();  
        }  
    }  
}
```